

AFRL-SN-WP-TR-2002-1174

**NONTHERMIONIC CATHODE
DEVELOPMENT**



M. A. Hasan

**The University of North Carolina at Charlotte
Department of Electrical and Computer Engineering
The Cameron Applied Research Center
Charlotte, NC 28223-0001**

OCTOBER 2002

Final Report for 23 January 1998 – 24 June 2002

Approved for public release; distribution is unlimited.

**SENSORS DIRECTORATE
AIR FORCE RESEARCH LABORATORY
AIR FORCE MATERIEL COMMAND
WRIGHT-PATTERSON AIR FORCE BASE, OH 45433-7318**

NOTICE

USING GOVERNMENT DRAWINGS, SPECIFICATIONS, OR OTHER DATA INCLUDED IN THIS DOCUMENT FOR ANY PURPOSE OTHER THAN GOVERNMENT PROCUREMENT DOES NOT IN ANY WAY OBLIGATE THE U.S. GOVERNMENT. THE FACT THAT THE GOVERNMENT FORMULATED OR SUPPLIED THE DRAWINGS, SPECIFICATIONS, OR OTHER DATA DOES NOT LICENSE THE HOLDER OR ANY OTHER PERSON OR CORPORATION; OR CONVEY AND RIGHTS OR PERMISSION TO MANUFACTURE, USE, OR SELL ANY PATENTED INVENTION THAT MAY RELATE TO THEM.

THIS REPORT HAS BEEN REVIEWED BY THE OFFICE OF PUBLIC AFFAIRS (ASC/PA) AND IS RELEASABLE TO THE NATIONAL TECHNICAL INFORMATION SERVICE (NTIS). AT NTIS, IT WILL BE AVAILABLE TO THE GENERAL PUBLIC, INCLUDING FOREIGN NATIONS.

THIS TECHNICAL REPORT HAS BEEN REVIEWED AND IS APPROVED FOR PUBLICATION.

/s/

MARK C. CALCATERA, Chief
RF Components Branch
Aerospace Components Division

/s/

ROBERT T. KEMERLEY, Chief
Aerospace Components Division
Sensors Directorate

Do not return copies of this report unless contractual obligations or notice on a specific document require its return..

REPORT DOCUMENTATION PAGE					Form Approved OMB No. 0704-0188	
<p>The public reporting burden for this collection of information is estimated to average 1 hour per response, including the time for reviewing instructions, searching existing data sources, gathering and maintaining the data needed, and completing and reviewing the collection of information. Send comments regarding this burden estimate or any other aspect of this collection of information, including suggestions for reducing this burden, to Department of Defense, Washington Headquarters Services, Directorate for Information Operations and Reports (0704-0188), 1215 Jefferson Davis Highway, Suite 1204, Arlington, VA 22202-4302. Respondents should be aware that notwithstanding any other provision of law, no person shall be subject to any penalty for failing to comply with a collection of information if it does not display a currently valid OMB control number. PLEASE DO NOT RETURN YOUR FORM TO THE ABOVE ADDRESS.</p>						
1. REPORT DATE (DD-MM-YY) October 2002		2. REPORT TYPE Final		3. DATES COVERED (From - To) 01/23/1998 – 06/24/2002		
4. TITLE AND SUBTITLE NONTHERMIONIC CATHODE DEVELOPMENT				5a. CONTRACT NUMBER F33615-98-C-1205		
				5b. GRANT NUMBER		
				5c. PROGRAM ELEMENT NUMBER 62204F		
				5d. PROJECT NUMBER 2002		
6. AUTHOR(S) M. A. Hasan				5e. TASK NUMBER 02		
				5f. WORK UNIT NUMBER AV		
7. PERFORMING ORGANIZATION NAME(S) AND ADDRESS(ES) The University of North Carolina at Charlotte Department of Electrical and Computer Engineering The Cameron Applied Research Center Charlotte, NC 28223-0001				8. PERFORMING ORGANIZATION REPORT NUMBER		
9. SPONSORING/MONITORING AGENCY NAME(S) AND ADDRESS(ES) Sensors Directorate Air Force Research Laboratory Air Force Materiel Command Wright-Patterson Air Force Base, OH 45433-7318				10. SPONSORING/MONITORING AGENCY ACRONYM(S) AFRL/SNDM		
				11. SPONSORING/MONITORING AGENCY REPORT NUMBER(S) AFRL-SN-WP-TR-2002-1174		
12. DISTRIBUTION/AVAILABILITY STATEMENT Approved for public release; distribution is unlimited.						
13. SUPPLEMENTARY NOTES Report contains color.						
14. ABSTRACT (Maximum 200 Words) This project focused on developing methods for fabrication of nonthermionic cold cathodes based on a lattice-matched material system consisting of a conducting substrate (source of electrons), a wide-bandgap semiconductor (conduction band closer to the vacuum level), and a low-work function material (to facilitate high emission of electrons). A material system fulfilling these requirements was found in indium phosphide (InP) as a substrate, cadmium sulfide (CdS) as the wide-bandgap semiconductor, and lanthanum monosulfide (LaS) as the low-work-function material. Growth of CdS was conducted using three methods: low-energy, ion-assisted growth (LEIAG); solid-source molecular beam epitaxy (SS-MSB); and gas-source MBE (GS-MBE). In situ reflection, high-energy electron diffraction (RHEED) indicated that growth of the desired epitaxial cubic-CdS occurred over a wide range of temperatures. However, surface decoration of hydrogen during GS-MBE resulted in initiation of hexagonal CdS phase as the layer grew thicker. Auger electron microscopy (AES) depth profiling showed stoichiometric composition of CdS and abrupt CdS/InP interfaces, while atomic force microscopy (AFM) showed small surface roughness, depending on the deposition method used. Thin layers of LaS were also grown on CdS. Further work will be needed to develop processing techniques for a testable electron emitter.						
15. SUBJECT TERMS cold cathode; nonthermionic cathode; solid-state emitter; negative electron affinity; cadmium sulfide; lanthanum sulfide; molecular beam epitaxy; low-energy, ion-assisted growth						
16. SECURITY CLASSIFICATION OF:			17. LIMITATION OF ABSTRACT: SAR	18. NUMBER OF PAGES 64	19a. NAME OF RESPONSIBLE PERSON (Monitor) Mark Calcaterra	
a. REPORT Unclassified	b. ABSTRACT Unclassified	c. THIS PAGE Unclassified			19b. TELEPHONE NUMBER (Include Area Code) (937) 255-4831 x3380	

Table of Contents

Section	Page
List of Figures	iv
List of Tables	vi
PART 1: PREPARATION AND OPTIMIZATION	1
1.0 INTRODUCTION	2
1.1 Understanding of the Problem.....	2
1.2 Background/Scope	2
1.3 Setup of Experiment and Initiation of the Project	6
1.3.1 MBE System Configuration and Setup	6
2.0 CONSTRUCTION AND CHARACTERIZATION OF A LOW-ENERGY, UHV- COMPATIBLE ION SOURCE	8
2.1 Ion Source Construction and Components	8
2.2 Characterization of the Ion Source.....	9
2.2.1 Pressure dependence	9
2.2.2 Dependence on Discharge Voltage	10
2.2.3 Dependence on Cathode (Filament) Current.....	11
2.2.4 Ion Extraction Mechanism and Dependence on Acceleration Voltage	12
2.2.5 Optimal Operation of the Ion Source	13
2.3 Magnetic Enhancement of the Ion Source.....	14
2.3.1 The Need for Higher Ion Current	14
2.3.3 Magnetic Enhancement of the Plasma	14
2.4 Characterization of the Ion Source Under Magnetic Enhancement.....	15
2.4.1 Dependence on Pressure	15
2.4.2 Dependence on Discharge Voltage, Filament Current (Cathode Temperature), and Acceleration Voltage.....	17
3.0 CD EVAPORATION SOURCE (EFFUSION CELL)	19
3.1 Monitoring and Calibration of the Cd Flux.....	20
3.2 Construction of a Movable Ion Gauge for Monitoring Cd Flux	22
4.0 DESIGN AND CONSTRUCTION OF A COMPACT, INDEPENDENTLY PUMPED EVAPORATION SOURCE FOR LA.....	24
PART 2: GROWTH AND DEVICE FABRICATION.....	28
5.0 ION-ASSISTED DEPOSITION USING SINGLE-GRID ION SOURCE.....	29
5.1 Initial Experiments: Deposition on Si(100).....	29
5.2 Problems and Challenges Associated With the Use of Ion-Assisted Deposition.....	32
6.0 DEPOSITION OF CDS USING RF ATOMIC SOURCE.....	33
6.1 The RF atomic source.....	33
6.2 Deposition of CdS on InP(100) Substrates	37
6.2.1 Surface Roughness of Grown Layers.....	39
6.2.2 Stoichiometry of Grown Layers.....	44
7. DEPOSITION OF CDS USING CDS SOLID-SOURCE.....	46
8. DEPOSITION OF LAS	47
9. SUMMARY	48
ACKNOWLEDGMENT	49
REFERENCES	50
List of Anonyms and abbreviations	52

List of Figures

Figure	Page
Figure 1. A schematic showing the proposed planar heterojunction cold cathode emitter in which the band diagram of the device is also shown. See references 1 and 2 for detailed theoretical calculation and description of the system.	3
Figure 2. Relationship of bandgap energy and lattice constant for group II-VI, including Si, Ge, InP, and GaAs. A wide range of tunable bandgaps and lattice constants can be achieved by using ternary and quaternary alloys.	4
Figure 3. A schematic showing the MBE system used in the current experiments	7
Figure 4. Schematic showing the low-energy, ultrahigh vacuum compatible ion source.....	8
Figure 5. The relationship between the discharge current and the discharge pressure for two filament currents: $I_f=7.5$ A and 8 A.....	10
Figure 6. Dependence of discharge current on discharge voltage for seven pressure values at constant filament current	11
Figure 7. Dependence of the discharge current I_d on the filament current for various pressure values	12
Figure 8. Relationship between the ion current emitted from the source and the acceleration voltage is shown for discharge pressures ranging from $P=2 \times 10^{-4}$ to 1×10^{-3} mbar.....	13
Figure 9. The change in the discharge current with increasing H_2S pressure in chamber for three values of the filament current.....	16
Figure 10. The dependence of the discharge current on the discharge voltage for several H_2S pressures.....	18
Figure 11. The dependence of discharge current on the cathode current (cathode temperature) for various discharge pressures.....	18
Figure 12. A schematic showing the Cd effusion cell.....	20
Figure 13. Schematic showing the wafer assembly used for calibration of the deposition rate from the Cd effusion cell.....	21
Figure 14. A schematic showing the setup needed for mounting a sensor to measure the deposition rate of Cd at the sample location	22
Figure 15. A schematic of the movable ion gauge	23
Figure 16. A schematic showing the design of the RF source	25
Figure 17. The La source fitted with resistive W heater	26
Figure 18. The La source fitted with conducting crucible made of Ta in which the crucible or the heater is biased (0-1000V) to facilitate electron irradiation of the crucible resulting in high cell temperature.....	27
Figure 19. AES depth profile of the CdS layer grown on Si(100) under the conditions described in the text.....	30
Figure 20. AES spectra from the surface of the sample as received (a) and after sputtering for 1 second (b).....	30
Figure 21 SEM image taken from the same sample.....	31
Figure 22. AFM image from the same sample taken from a $5 \mu m$ by $5 \mu m$ area	31
Figure 23. A schematic of the RF source used in the current experiments.....	34
Figure 24. The experimental setup used for spectra measurements from the RF source.....	34
Figure 25. Typical spectra from the RF atomic source	35

List of Figures (Continued)

Figure	Page
Figure 26. The dependence of the atomic S peak-intensity, which is related to the atomic S concentration, on the RF power for two H ₂ S gas pressures.....	36
Figure 27. The dependence of S atomic fraction on the gas pressure at a RF power of 350 W	36
Figure 28. RHEED pattern taken from (a) clean InP(100)2x1 and (b) after growth of CdS	37
Figure 29. AES depth profile from a CdS layer grown on InP(001) substrate at T _s = 150 °C	38
Figure 30. AFM image over 8x8 μm ² taken from a CdS layer grown at T _s = 350 °C.....	38
Figure 31. The dependence of growth rate on the Cd cell temperature in the figure.....	39
Figure 32. AFM image of a 275-Å-thick CdS layer grown at 150 °C.....	40
Figure 33. AFM of a 2000-Å-thick layer grown at 150 °C	41
Figure 34. The average surface roughness as a function of the layer thickness	42
Figure 35. The average surface roughness as a function of the growth temperature.....	42
Figure 36. The average surface roughness as a function of the RF power used in the S atomic source.....	43
Figure 37. The average surface roughness is shown as a function of H ₂ S pressure used during growth	43
Figure 38. Cd and S concentration in layers grown in the temperature range from 150 to 300 °C	44
Figure 39. Dependence of layer compositions on the RF power used.....	45
Figure 40. Dependence of layer composition on H ₂ S gas pressure during growth.....	45
Figure 41. RHEED pattern from CdS grown by SS-MBE.....	46
Figure 42. Deposition rate of CdS from CdS solid source.....	47

List of Tables

Table	Page
Table 1. The Structure, Bandgap, and Other Relevant Parameters of Group II-VI Materials.....	5
Table 2. Auger analysis of the CdS film.	30

PART 1: PREPARATION AND OPTIMIZATION

1.0 INTRODUCTION

1.1 Understanding of the Problem

Impetus for development of cold cathodes has been provided primarily by their applications as matrix-addressable electron microguns for field emission flat panel displays and as compact and efficient electron sources for microwave power amplifier tubes. For flat panel displays, required electron emission currents are in the modest range of 10 to 100 μA per pixel, which are achievable with gated microtip field emitter arrays (FEAs) for gate voltages in the range of 10 to 50 V. On the other hand, cathodes for certain microwave power amplifier tubes need to exhibit emission currents on the order of 1 A with current densities approaching 100 A/cm^2 . Only moderate success has been achieved so far in the use of FEA cathodes for this application, with reliability, thermal management and lifetime being the primary challenges. Due to the planar geometry and more robust structure, especially under ion bombardment during the device operation, solid-state emitters might be better suited for high-current-density applications than for microtip FEAs. Successful development of such electron emitters suitable for replacement of thermionic cathodes in microwave power amplifiers would affect a number of military and commercial products, such as transmitters for radars, televisions, tropospheric scatters, ground-to-satellite, earth-to-spacecraft, and illuminators for guided missiles as well as microwave heating and wireless communications [6,7]. Microwave power tubes still remain the only available technology for high-power and high-frequency amplifier applications.

1.2 Background/Scope

Traditionally, electron emitters are made of sharp tips of metals or low work-function materials such as W and LaB_6 operated at high temperature. This tradition has been carried out to vacuum microelectronics where the dominating technology utilizes a cone-type gated field emitter in which the emitter is made of either a metal (commonly Mo) or a semiconductor (Si, diamond, AlGaN , GaAs). While cone-type (tip) FEAs have been successfully fabricated and tested, there is a growing trend toward the fabrication of multilayer planar field emitters that utilize electron tunneling through wide-bandgap semiconductors [1,2, 8-13]. The latter class of planar field emitters offers a considerable decrease in processing complexity, a better thermal management, and the advantages of lower operating voltages. However, the wide-bandgap semiconductor layer should be of good quality and thin enough so that electron scattering is not significant and the device is capable of withstanding the applied voltage.

Recent calculations by Mumford and Cahay [1,2] have shown an extremely attractive and well-thought system of II-VI compounds for planar field emission technology. The proposed device is based on electron tunneling through a thin layer of wide-bandgap cadmium sulfide (CdS) into a semimetallic, low-work-function lanthanum sulfide (LaS) layer that facilitates the emission of electrons into vacuum (see Figure 1).

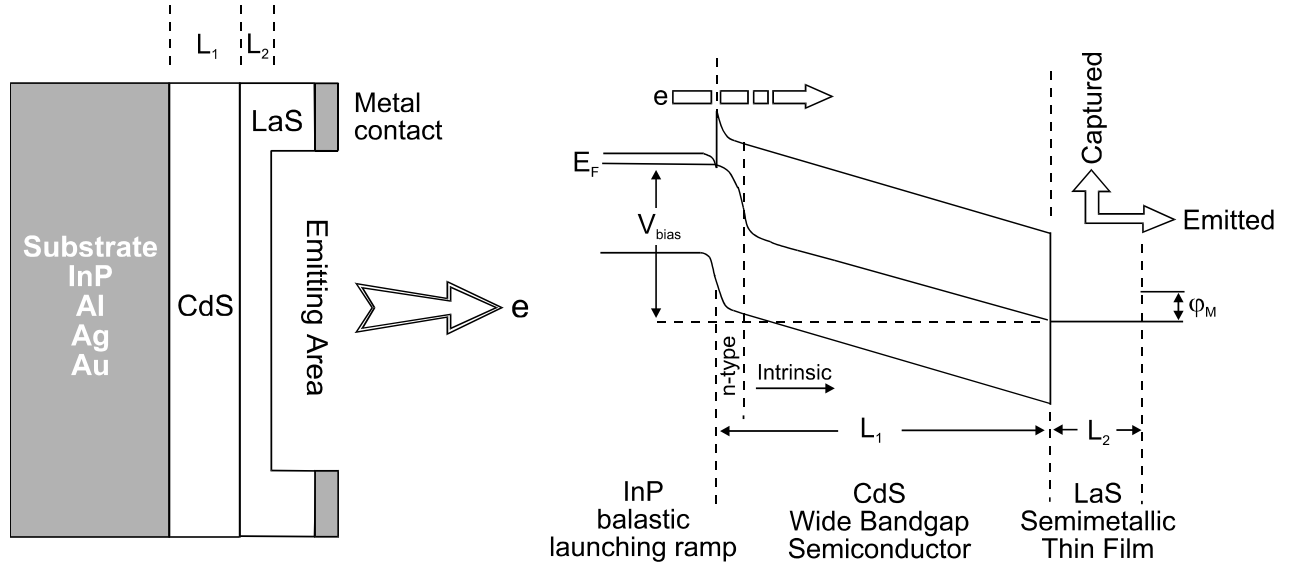


Figure 1. A schematic showing the proposed planar heterojunction cold cathode emitter in which the band diagram of the device is also shown. See references 1 and 2 for detailed theoretical calculation and description of the system.

The proposed structure is capable of low voltage operation (< 20 V) and high emission current approaching several hundred A/cm^2 . In addition, the proposed materials comprise a highly lattice-matched system (see Figure 2 and Table 1), a condition that alleviates the major obstacle in achieving high quality epitaxial growth. For growth on InP ($a_{\text{InP}} = 5.869$), the lattice mismatch η is only 0.6 percent. InP substrates have the additional advantage, compared to GaAs, of higher thermal conductivity, which is a requirement for high-power operation. For growth on metals (Al, Ag, and Au), lattice match can be achieved if the CdS lattice is rotated by 45° with respect to the metal lattice ($\eta_{\text{Al}} = 1.7$ percent, $\eta_{\text{Ag}} = 0.7$ percent, $\eta_{\text{Au}} = 0.98$ percent after 45° rotation). Epitaxial growth in which rotational epitaxial-relationship or multiple lattice match is fulfilled has been reported in the literature [3-5,14-16]. One example is growth of Al(100) on Ge(100) where the Al(100) crystal is rotated by 45° with respect to the Ge(100) lattice ($\eta = 1$ percent taking the rotation into account) [15]. This class of epitaxy has been treated theoretically by Zur and McGill [14]. They showed that heteroepitaxy can be achieved by matching n lattice translations of the film to m translations of the substrate and presented experimental examples for growth of CdTe(111) on GaAs(100) and CdTe(111) on Al_2O_3 . Al(110) growth on Si(100) [3] and Al(111) on Si(111) [4,5] reported by the PI of this effort are additional examples of this type of epitaxy. An example for translational symmetry with no rotation is the cases of Fe growth on ZnSe and ZnSe on Fe [16]. The lattice constant of ZnSe is almost twice that of iron.

This work, aims at solving the scientific and technological issues related to the growth of CdS and LaS, and the fabrication of heterojunction cold cathodes (HCC).

Historically, the development of active device structures in group II-VI materials has been hampered, for a long period of time, by difficulties in achieving control over background impurities and doping of these materials [17,18]. The advent of molecular beam epitaxy (MBE) [19-21], metal-organic molecular beam epitaxy (MOMBE) [22-25], and metal-organic chemical vapor deposition (MOCVD), have brought about new generation of these materials with impurity backgrounds in the range of 10^{14} to 10^{15} cm^{-3} and controllable doping levels up to $\sim 10^{18} \text{ cm}^{-3}$. These advancements have resulted in the latest breakthroughs in the fabrication of light-emitting

devices, such as light-emitting-diodes (LEDs) and semiconductor lasers [26-28], transistors, and detectors. Both Sony and 3M/Phillips put considerable research and development (R&D) efforts to establish reliable semiconductor lasers made of group II-VI materials for commercial applications.

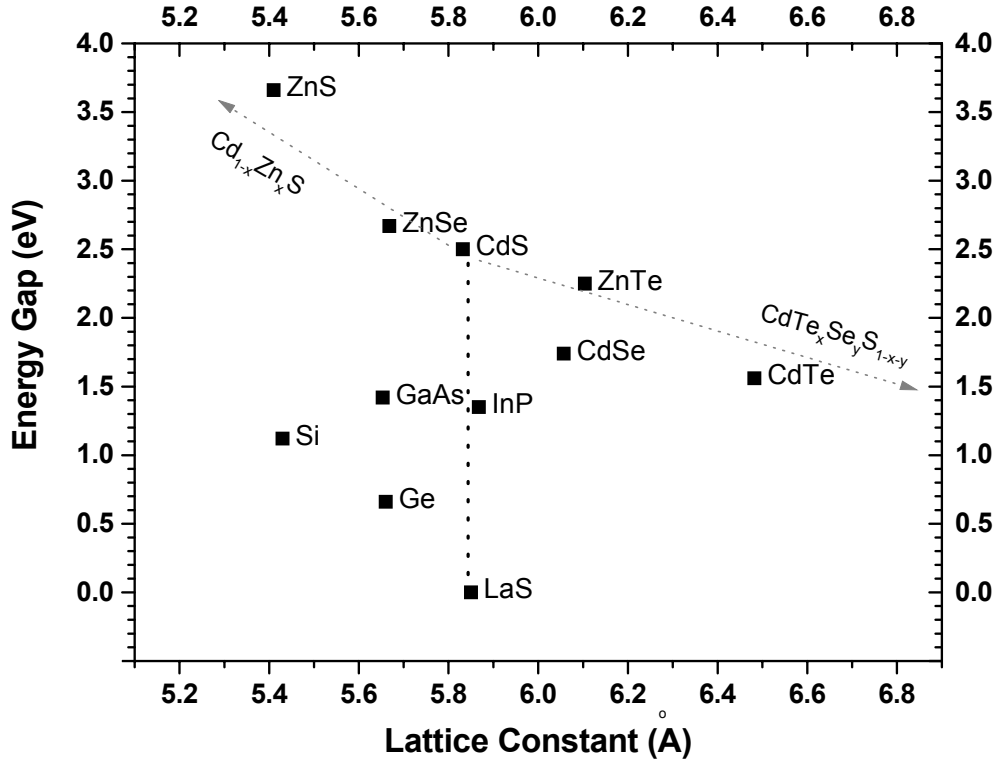


Figure 2. Relationship of bandgap energy and lattice constant for group II-VI, including Si, Ge, InP, and GaAs. A wide range of tunable bandgaps and lattice constants can be achieved by using ternary and quaternary alloys.

Figure 2 shows the bandgap and the lattice parameters for the cubic phases of II-VI compounds together with LaS, Si, Ge, InP, and GaAs, while Table 1 summarizes some of the properties of group II-VI and other relevant materials. As can be seen in Figure 2, various combinations of these materials can result in a large window of tunable bandgap energies and lattice constants. The bulk of the work on II-VI compounds, up till now, has been carried out on growth of ZnSe with fractional incorporation of S, Cd, and Mg in order to engineer the required bandgap offsets, refractive index, and lattice match. The central theme of most of the work is the fabrication of LEDs and lasers [17]. The choice of ZnSe as the main compound is related to a few practical factors. ZnSe has a close lattice match to GaAs, which has been commercially available as a substrate having a high degree of perfection. The availability of high quality substrates is a crucial factor for the development of any material system. The other important factor is the wide bandgap of ZnSe, which makes it suitable for short-wavelength application. Finally, Zn and Se

fluxes are easier to control compared to S, which has an extremely high vapor pressure ($\sim 2 \times 10^{-6}$ torr at room temperature). However, with the current deposition technology, problems with high vapor pressure materials can be handled by using valved cracker-cells with dual temperature zones. In this case, sulfur is supplied to the substrate as needed and the sulfur source can be isolated from the deposition chamber so that ultra-high vacuum (UHV) condition can be attained and layers with no S content can be grown, if required.

Table 1. The Structure, Bandgap, and Other Relevant Parameters of Group II-VI Materials

Materials	Structure	Bandgap (eV) 300 K	a (Å)	c (Å)	Donors, E_i (meV)	Acceptors, E_i (meV)	Mobility* μ_n μ_p	Refractive Index
CdS	W	2.42	4.133	6.710	Ga, 33.1	Li, 165	500 -	2.5
	Z	2.5	5.832		Cl, 32.7	Na, 169		
LaS	R		5.850					
ZnS	W	3.80	3.820	6.260	Al, 100	Na, 190	150 -	2.8
	Z	3.66	5.410					2.4
ZnSe	Z	2.67	5.668		Al, 25.6	Li, 114 N, 111	500 80	2.8
ZnTe	Z	2.25	6.104		Al, 18.5 Cl, 20.1	Li, 60.5 P, 63.5	340 100	3.1
ZnO	W	3.2	3.250	5.207	In, 50 Al	Cu, 190 Li, 150	200 -	2.0
CdSe	W	1.74	4.299	7.015	X, 19.5	Li, 109	600 -	2.6
	Z		6.057			P, 83		
Si	D	1.12	5.430		P, As, Sb	B,Al,Ga,In	1450, 500	3.42
Ge	D	0.66	5.646		“	“		
InP	Z	1.35	5.869		S	Cd		

Z = Zinc Blend, W = Wurtzite, D = Diamond, R = Rocksalt

* Mobility values are given for 300 K in $\text{cm}^2/\text{V} \cdot \text{sec}$

Due to the above factors, growth of CdS has received much less attention. Cd and S were incorporated in ZnSe layers in order to adjust the bandgap and the lattice constant of the grown layers. However, the commercial availability of device quality InP wafers have brought about a renewed interest in CdS growth [29-31], but no established epitaxial growth procedures have yet been reported. Most of the reports show defective and multiphase growth of CdS mainly due to an inherent problem with the growth methods used. It is part of our mission to investigate and develop reliable and reproducible methods for epitaxial growth of high quality CdS and LaS layers. Establishing the epitaxial technology is a must for the development and fabrication of active devices. This relationship has been the norm for all established technologies such as Si and GaAs.

1.3 Setup of Experiment and Initiation of the Project

This project was off to a good start. First, we won a space for our MBE system in the clean room facility. Second, the Cameron Applied Research Center (CARC) agreed to fund installation of all the necessary power, water, and gas lines to the MBE system and its control units. Third, the MBE system was installed in a rather short time and many of the requested components were purchased and installed. Fourth, our students made substantial progress in repairing our mask generator, which gave us the in-house capability of designing and modifying the required masks for the field emitter fabrication.

1.3.1 MBE System Configuration and Setup

The MBE system was made by VG-Scientific, which is one of the best manufacturers of MBE systems. A schematic of the system is shown in Figure 3. The system consists of three main chambers: deposition, analysis, and load-lock.

The deposition chamber contains provisions for up to eight material delivery and manipulation sources, such as effusion cells, ion sources, radio frequency (RF) atomic sources, photon sources, etc. It also contains ports for mass spectrometry, reflection high-energy electron diffraction (RHEED), quartz microbalance, view ports, and ion gauges. The inner surface of the deposition chamber is protected by liquid nitrogen (LN_2) shroud in order to reduce the pressure around the sample by adsorbing residual-gas molecules and minimizing any heating effects generated during heating the sample or the evaporation sources. The pumping effect of the LN_2 shroud is further enhanced by a titanium sublimation pump (TSP), which is mounted inside the upper portion of the LN_2 shroud. The sample holder is rotatable around the sample normal and can be modified to accommodate up to 4 inch-diameter wafer. In the current configuration, the sample holder was set to handle 3 inch diameter wafers. The sample heater, which is made of Ta strips heated resistively by passing current through the strips, can be programmed to achieve a sample temperature as high as 950°C . The substrate temperature is measured by an infrared (IR) pyrometer mounted to on the view ports. The deposition chamber also contains an effusion cell for Cd (described Section 3, Part 1), an ion source for H_2S (described in Section 2, Part 1), an RF atomic source for H_2S (see Section 6.1, Part 2), and a CdS effusion cell for direct deposition from CdS solid source. The details of the system's setup are shown schematically in Figure 3.

The analysis chamber is integrated with the load-lock chamber and contains provisions for Auger electron spectroscopy (AES) using hemispherical analyzer model CLAM2 from Vacuum Generators (VG), low-energy electron diffraction (LEED), and a sample transfer system capable of moving the samples from the load-lock chamber to the deposition chamber or the analysis station. In addition, the analysis chamber contains many ports for possible addition of other analytical tools and sample treatment prior to or after growth.

The load-lock chamber, while integrated with the analysis chamber, is isolated from the analysis chamber by a built-in gate valve that combines the functions of a valve and a sample-magazine holder. The sample magazine is capable of holding ten 3 or 4 inch-diameter wafers. In a typical operation, 10 samples are loaded into the sample magazine and stored in the system for sequential use. This prevents exposure of the load lock to atmosphere every time a sample is loaded into the

system. In turn, the vacuum in the entire system is improved and the possibility of contamination is reduced.

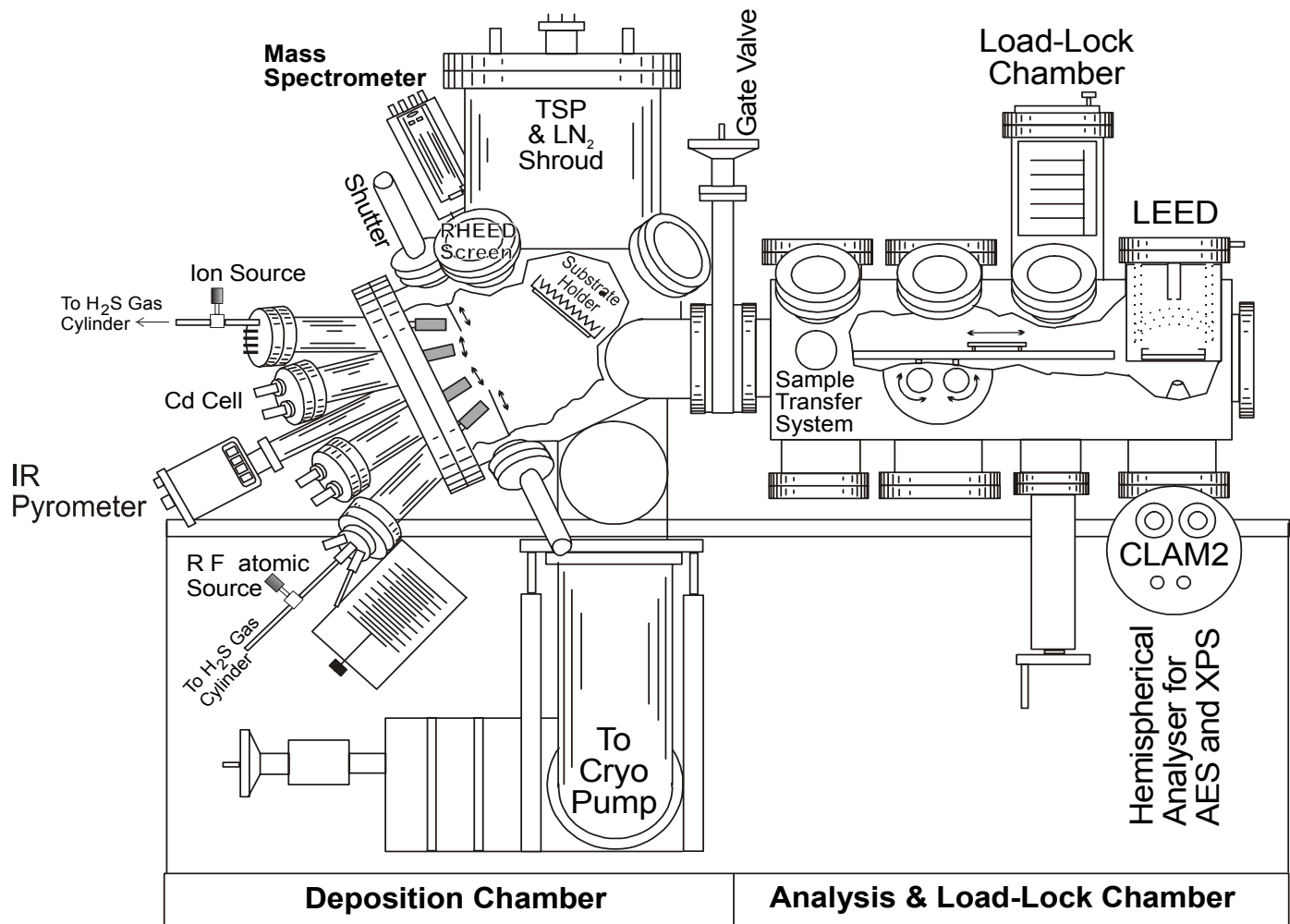


Figure 3. A schematic showing the MBE system used in the current experiments

2.0 CONSTRUCTION AND CHARACTERIZATION OF A LOW-ENERGY, UHV-COMPATIBLE ION SOURCE

A low-energy, ultrahigh-vacuum-compatible ion source was designed and built for this work. We have installed the ion source in a test vacuum chamber in order to characterize the source and establish its mode of operation prior to installation into the MBE system. A schematic for the ion source and its control circuit is shown in Figure 4.

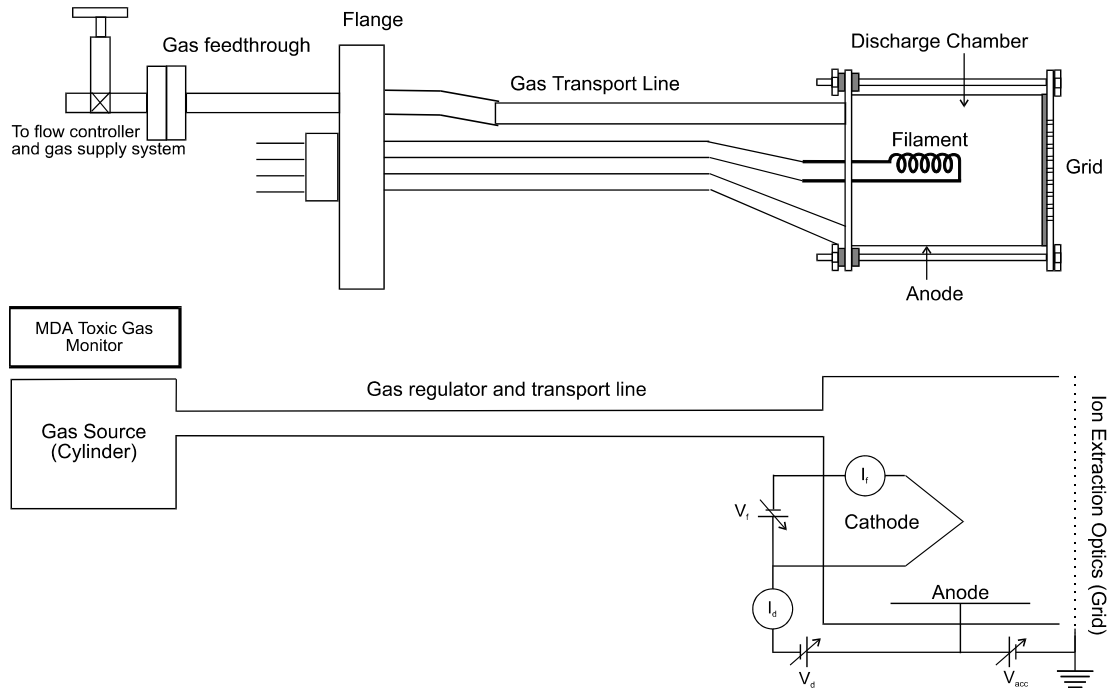


Figure 4. Schematic showing the low-energy, ultrahigh vacuum compatible ion source

2.1 Ion Source Construction and Components

The ion source consists of three major components:

- 1. Cathode:** is made of a tungsten (W) wire heated resistively to a high temperature in order to stimulate emission of electrons. In the current design, we have utilized a V-shaped W filament for the cathode. The current configuration has a filament 0.25 mm in diameter. Smaller diameter filaments burn easier after a short operation time, while filaments of larger diameter require much higher current to heat the filament in order to achieve the same emission current.

- 2. Anode:** is a metal cylinder surrounding the cathode. It is biased negatively with respect to the cathode. The potential difference between the anode and cathode is called the discharge potential (V_d). Electrons emitted from the cathode are accelerated toward the anode by the applied

potential. During this excursion, electrons may collide with atoms and molecules and lose part or all of their energy, resulting in the ionization of atoms/molecules.

3. Ion optics: serve two major functions: a) extract ions from the plasma formed between the anode and cathode, and b) focus the ion beam into the substrate. In the present design, we have excluded the focusing component since we are looking for a broad ion beam that can cover the whole substrate area. Ion extraction is made by a W metal grid that is biased negatively with respect to the anode. The grid was grounded and the anode potential was raised to the required ion energy (acceleration voltage, V_{acc}).

Gas is fed to the ion source through a regulated leak valve connected to the ion source flange through 1.33 inch flange.

2.2 Characterization of the Ion Source

To determine the behavior of the ion source and its optimal operating conditions, the relationship between the ion current, discharge current, filament current, and pressure must be determined.

2.2.1 Pressure dependence

Figure 5 shows the relationship between the discharge current (I_d) and the discharge chamber pressure (P) for two values of filament current. At low pressures ($< 10^{-4}$ mbar), I_d increased slowly with increasing P . I_d then increased rapidly in a narrow pressure range (9×10^{-5} mbar $< P < 2 \times 10^{-4}$ mbar), reaching saturation at higher chamber pressures. The dependence on the pressure was the same for the three filament current values examined in this experiment. However, for filament current $I_f = 8$ A, the discharge current is higher in the saturation region ($P > 2 \times 10^{-4}$). This is due to a higher rate of electron emission from the filament at higher filament temperature (higher filament current). In this regime, plasma was established, resulting in the formation of a negative glow region around the filament (cathode) that acted as a virtual anode. The virtual anode is separated from the filament by the dark space (sheath). Since the plasma potential is within a few electron volts from the anode potential, most of the discharge potential was dropped across the width (d) of the dark space resulting in a high electric field (E_d) across the sheath ($E_d = V_d/d$). This then leads to a more efficient extraction of electrons from the dark space around the filament into the plasma. Thus, in this regime, the discharge current is limited by the thermionic emission from the filament. The dark space width, d , typically ranges from a fraction of a millimeter to a few millimeters, depending on the pressure, type of gas, and the discharge voltage. Increasing P does not only increase the ionization cross section due to decreased mean free path for ionizing collisions, but also decreases the dark space thickness, d , around the filament, resulting a stronger electric field E_d .

For $P < 10^{-4}$ mbar, there is no plasma formed, and the applied voltage is distributed linearly between the anode and the cathode (~ 1 cm in our case), which results in a low applied field in the vicinity of the cathode causing low emission current (emission is space-charge limited). The combined effects of low emission and low pressure result in low ionization events and, thus, low discharge current.

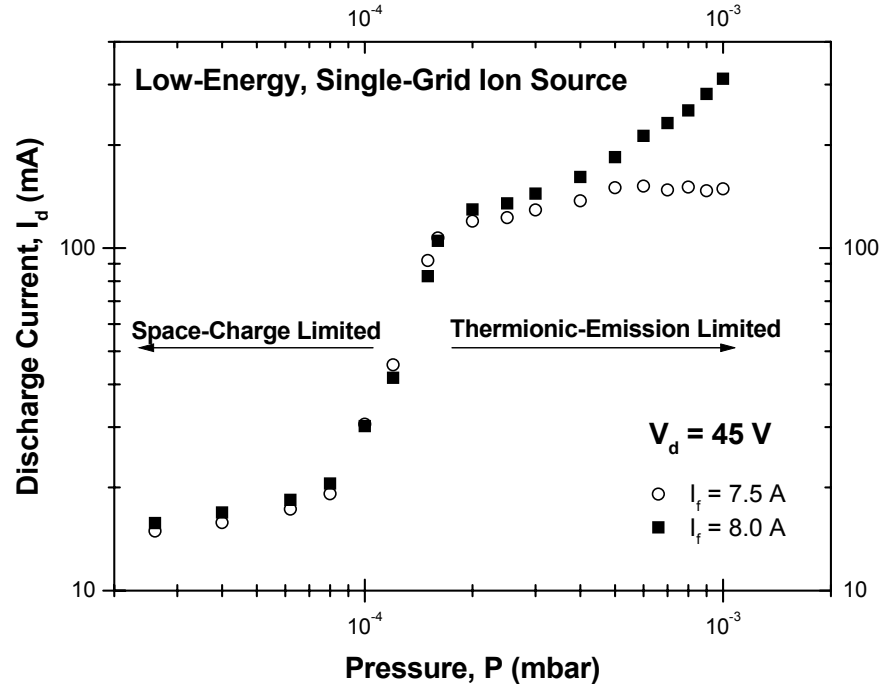


Figure 5. The relationship between the discharge current and the discharge pressure for two filament currents: $I_f = 7.5$ A and 8 A

2.2.2 Dependence on Discharge Voltage

The dependence of I_d on the discharge voltage V_d for constant pressure values ranging from 2×10^{-5} to 8×10^{-4} mbar is shown in Figure 6. At low pressures ($P < 1 \times 10^{-4}$ mbar), I_d increased slowly with increasing V_d throughout the voltage range investigated (0 to 70 V) consistent with the pressure dependence shown in Figure 5. In this range, I_d is space charge limited. At higher pressures, plasma was initiated with a turn-on voltage, V_{on} , that decreased with increasing pressure, P , as expected. V_{on} is typically measured by extrapolating the steep portion of the I_d versus V_d curve to the abscissa. In the high pressure range, the discharge current reaches saturation at high V_d values with a turn-over voltage (from the steeply rising portion to saturation) that decreases with increasing P . This is due to decreasing cathode sheath thickness, d (dark space thickness), with increasing pressure allowing the discharge potential to fall across narrower space (high E_d), which in turn enhances the extraction of electrons from the space charge region around the cathode. The latter process increases the ionization rate and thus the discharge current, I_d . The saturation in I_d indicates that the ionization process is limited by thermionic emission from the filament.

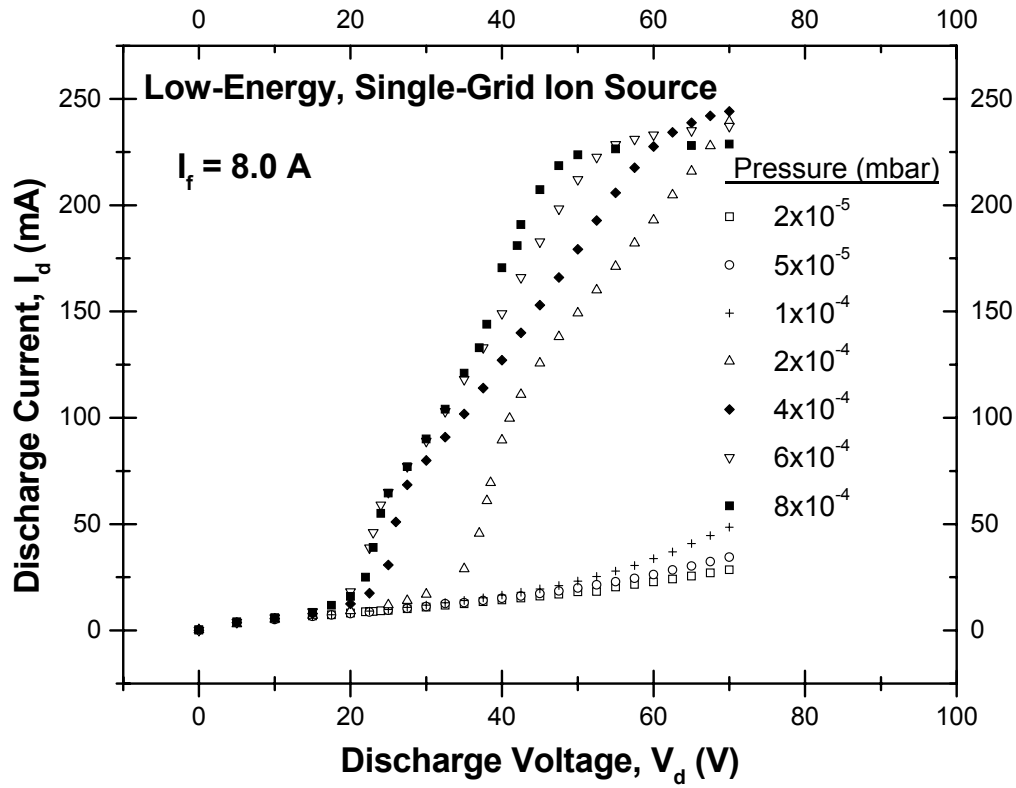


Figure 6. Dependence of discharge current on discharge voltage for seven pressure values at constant filament current

2.2.3 Dependence on Cathode (Filament) Current

The dependence of discharge current I_d on the filament current I_f at various pressure values, shown in Figure 7, is consistent with results shown in Figure 5 and Figure 6. For pressure values below $\sim 1 \times 10^{-4}$ mbar, no plasma is formed and electron emission is space-charge limited, as indicated by the weak dependence of I_d on I_f . At higher pressure values, plasma is initiated and I_d showed a strong dependence on I_f . For the full range of pressure investigated, the discharge current is negligible for low I_f values. This is due to low electron emission from the filament. Electron emission from the filament depends exponentially on the filament temperature. At low I_f values, the filament temperature is low and consequently electron emission is very low. At high I_f values and in the presence of plasma (high P and V_d), I_d is primarily controlled by I_f as shown in Figure 7. The discharge in this case is limited by thermionic emission from the filament.

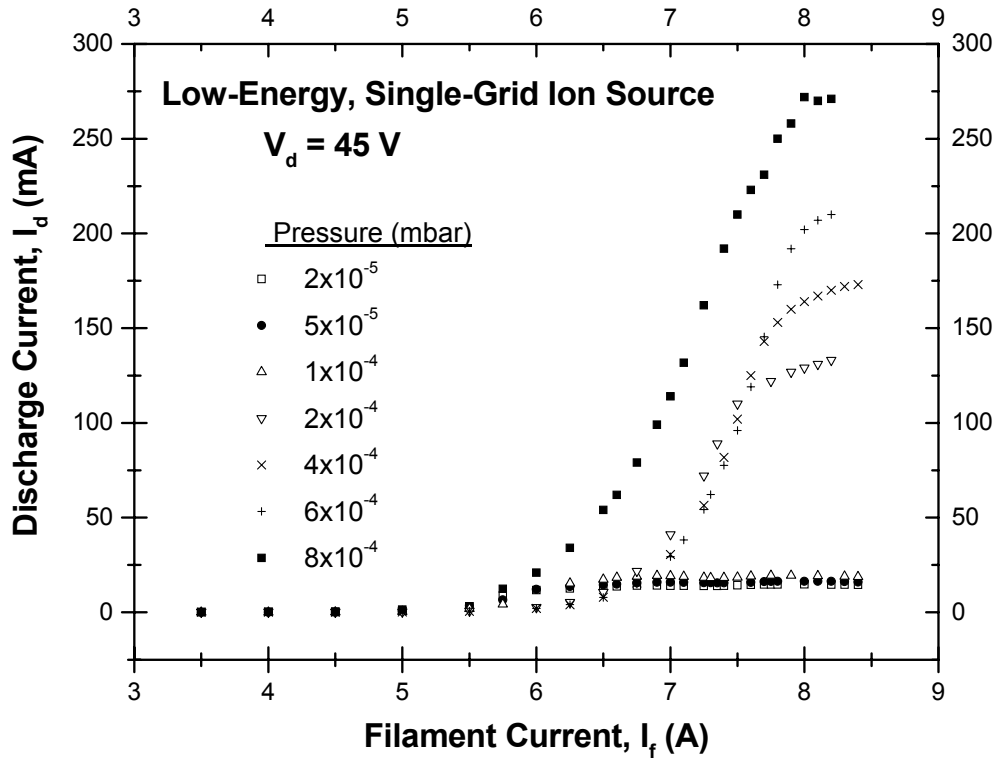


Figure 7. Dependence of the discharge current I_d on the filament current for various pressure values

2.2.4 Ion Extraction Mechanism and Dependence on Acceleration Voltage

In the current design, ion extraction was performed using a single grid made of tungsten (W) mesh (see Figure 4). When a potential is applied between the anode and the grid, positive ions are extracted from the plasma and accelerated toward the grid. Some ions are captured by the grid while the remainder escape through the grid holes toward the substrate, accounting for the measured ion current I_{ion} in these experiments. When the plasma is initiated, the actual energy of the ions equals the sum of the plasma potential, V_p , and the acceleration voltage, V_{acc} . Since V_p is typically of the order of a few electron volts, the ion energy is almost equal to V_{acc} . Figure 8 shows dependence of the ion current I_{ion} on the acceleration voltage V_{acc} (the upper portion and left axis) for operating pressures ranging from 2×10^{-4} to 1×10^{-3} mbar and V_{acc} up to 800 V. The ion current was measured using a 1 cm^2 probe mounted $\sim 10 \text{ cm}$ from the source. For pressure values below 2×10^{-4} mbar, the plasma was not ignited, and the ion current was very low (not practical for typical deposition experiments). The changes in the discharge current (the lower portion and right axis) for each pressure value were also recorded. For acceleration voltages, V_{acc} , $< 50 \text{ V}$, the ion current, I_{ion} , is typically below $1 \mu\text{A}$, which is not enough to achieve reasonable deposition rates. Above 50 V the ion current increased slowly, with increasing V_{acc} reaching a semi-saturation for $V_{acc} > 400 \text{ V}$. This behavior is expected since for a single-grid ion source, the ion current follows Child's law expressed as follows: $I = (4\epsilon_0/9)(2e/m)^{1/2} V^{3/2}/d$, where ϵ_0 is

permittivity of free space, e and m are the electron charge and mass respectively, $V = V_{acc}$, and d is the sheath thickness between the plasma and the grid. The discharge current, except for the lowest pressure value examined, remained almost constant irrespective of V_{acc} value.

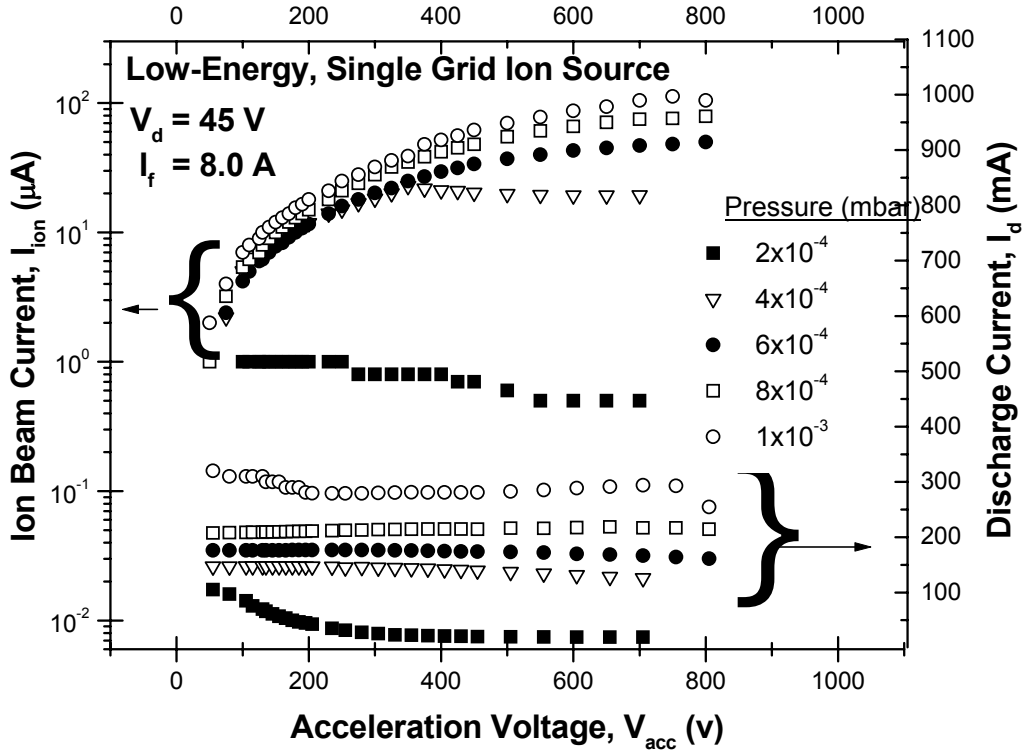


Figure 8. Relationship between the ion current emitted from the source and the acceleration voltage is shown for discharge pressures ranging from $P=2 \times 10^{-4}$ to 1×10^{-3} mbar

2.2.5 Optimal Operation of the Ion Source

The optimal operation of the source would be in a range of parameters in which the ion source is stable, i.e., away from the steep portions of the curves presented in Figure 5 to Figure 8. In addition, the ion current should be high enough to be practical for deposition applications. This would translate into the following parameters:

$$P > 1 \times 10^{-4} \text{ mbar}$$

$$V_d > 45 \text{ V}$$

$$I_f > 8 \text{ A}$$

$$V_{acc} > 50 \text{ V}$$

2.3 Magnetic Enhancement of the Ion Source

2.3.1 The Need for Higher Ion Current

The above characterization demonstrates a rather normal behavior of the ion source. However, to perform meaningful experiments at low acceleration voltages ($V_{\text{acc}} < 200$ eV), the emitted ion current, I_{ion} , must be increased to provide enough ions to sustain a reasonable growth rate. To illustrate this point, let us assume that the required deposition rate for an experiment is one monolayer per second (ML/s). This is a reasonable deposition rate for typical MBE experiments. For CdS(100), the lattice constant is equal to 5.832 Å, and the thickness of one ML accounts for 1.458 Å. Thus, the time required to deposit a 1000-Å-thick layer using a growth rate of one ML/s is equal to ~ 686 seconds (11 minutes and 26 seconds), which is very reasonable time. (Note that the experiment may require a few hours of careful preparation and few days in achieving UHV conditions, but these preparations can be used to produce many samples.) Now, let us calculate the ion flux needed to achieve a deposition rate of one ML/s.

- On the average, 0.5 ML of Cd + 0.5 ML of S is needed for each ML of CdS
- One ML of atoms on the CdS(100) surface = 5.88×10^{14} atoms/cm², then 0.5 ML = 2.94×10^{14} atoms/cm². The number of S ions/cm² per second emitted from the ion-source must then correspond to 0.5 ML/s.
- Since 1 ampere = 6.25×10^{18} ions/cm².s, 0.5 ML/s corresponds to a S⁺ ion current of ~47 μA.

However, only a fraction of H₂S is ionized, and the ion source emits both ions and neutral atoms as well as molecules. The simple calculation above assumes that only ions contribute to the deposition process. In reality, both ions and neutrals emitted from the ion source would contribute to growth with the ions being the major participants. Thus, the above calculated value represents an upper limit for the I_{ion} required to reach a deposition rate of one ML/s. Nevertheless, a close look at Figure 8 suggests the need for higher I_{ion} at low V_{acc} . Also, note that the ion current shown in Figure 8 was measured at a distance of ~ 10 cm from the source, while the sample is located ~ 30 cm from the source. This means that the actual ion current at the sample location is much less than the measurement at the probe.

2.3.3 Magnetic Enhancement of the Plasma

One way to increase the ion current is to enhance the plasma density in the ion source. A simple way to induce such an enhancement is to use a magnetic field in the discharge chamber. The magnetic field results in a helical electron trajectory, which enhances the ionization cross section of electrons. Electrons spend longer time in the discharge chamber before being captured by the anode, which increases the electrons' chances to encounter atoms and molecules, resulting in a greater ionization events.

Initially, we have tried using permanent magnets that were available to us in the laboratory. However, due to the heat generated by the filament, the magnets lost their strength after a short operation time.

We have implemented two alternatives:

1. Using a permanent magnet that is compatible with high temperature. Alnico magnets have very high energy for their size, and are very resistant for demagnetization. These magnets are composed of carbon-free, electrically conductive aluminum/nickel/cobalt steel alloys (Al/Ni/Co). They are characterized by excellent temperature stability (up to 525 °C), which makes them suitable for use around the discharge chamber of the ion source. Also, they are compatible with the UHV environment. We ordered these magnets through McMaster-Carr Company and tested the source. In the following subsection, a detailed characterization for the source will be presented.

2. Using a coil around the discharge chamber. We made an attempt to use Kapton coated wire around the discharge chamber. The reason for this choice is that Kapton coated wires, compared to using ceramic beads to insulate the wire, are thin, which allows a large number of turns in a small space. However, the vapor pressure of Kapton becomes very high above 150 °C, an effect that is not desirable in an MBE environment (results in contamination). To minimize heating of the coil, we have constructed a metal housing for the coil that sits around the discharge chamber. This modification resulted in enlarging the size of the ion source and frequent failures due to electrical shorting of the discharge chamber to the coil housing. While this approach may work for other experimental setups, it came to a road-block in our MBE chamber due to insufficient space in the mounting port for the ion source and the failure problems mentioned above.

As an alternative, we have used a bare wire with ceramic beads to insulate the turns of the coil from each other and from the discharge chamber. While the new design may look bulky with a small number of turns, it can be mounted directly on the discharge chamber, and a much higher current can be used to achieve higher magnetic field. We have tested the ion source with the new magnet. Though this alternative gave a little enhancement to the operation of the ion source, the gain in the ion current is still small.

From these tests, the first method of using permanent high-temperature magnets showed the best enhancement. The permanent magnet provides a compact solution for the problem, does not require feedthroughs to supply current to the coil, and will not result in additional heat generation due to the high current needed to generate the magnetic field in the coil.

2.4 Characterization of the Ion Source Under Magnetic Enhancement

2.4.1 Dependence on Pressure

Figure 9 shows the dependence of discharge current, I_d , on the pressure under magnetic enhancement. The general behavior of the I_d is similar to that of Figure 5 except for much higher current in the thermionic-emission limited regime (saturation area). The increase in I_d is mainly due to the presence of the magnetic field, which results in a long helical electron trajectory that increases the probability of electrons to ionize gas atoms as they travel between the cathode and the anode. The discharge current behavior is shown for three values of the filament current I_f ($I_f = 7.5, 8.0, 8.5$ A).

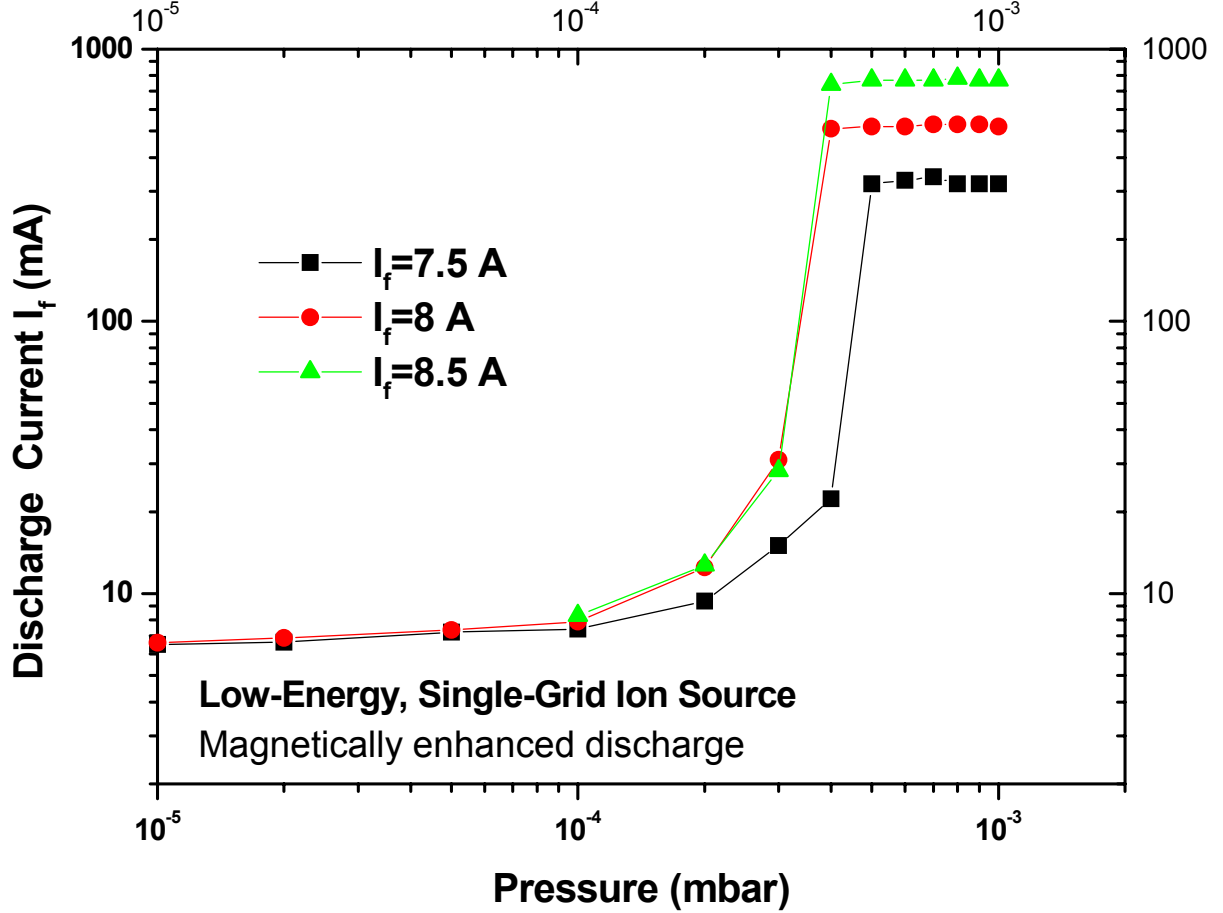


Figure 9. The change in the discharge current with increasing H_2S pressure in chamber for three values of the filament current

At low pressures ($< 10^{-4}$ mbar), I_d increased slowly with increasing P . I_d then increased rapidly in a narrow pressure range (9×10^{-5} mbar $< P < 2 \times 10^{-4}$ mbar), reaching saturation at higher chamber pressures. The dependence on the pressure was the same for the three filament current values examined in this experiment. However, the discharge current in the saturation region ($P > 2 \times 10^{-4}$) increased with increasing filament current. This is due to a higher rate of electron emission from the filament at higher filament temperature (higher filament current) in the presence of plasma. As explained earlier, in this regime, plasma was established, resulting in the formation of a virtual anode separated from the filament by the dark space (sheath), which is typically in the order of one to a few millimeters. This results in a high electric field (E_d) across the sheath ($E_d = V_d/d$) causing a more efficient extraction of electrons from the dark space around the filament into the plasma. This effect together with the enhancement in the ionization cross-section induced by the magnetic field result in observed enhancement in the discharge current

demonstrated in Figure 9. In this regime, the discharge current is limited by the thermionic emission from the filament.

For $P < 10^{-4}$ mbar, there is no plasma formed and the applied voltage is distributed linearly between the anode and the cathode (~ 1 cm in our case), which results in a low applied field in the vicinity of the cathode causing low emission current (emission is space charge limited). The combined effects of low emission and low pressure result in low ionization events and thus low discharge current. Even with the magnetic enhancement, the longer electron path is counteracted by the long mean free path of electrons in this pressure range.

2.4.2 Dependence on Discharge Voltage, Filament Current (Cathode Temperature), and Acceleration Voltage

Figure 10 shows the dependence of discharge current on the discharge voltage, while Figure 11 shows the dependence on filament current. The overall dependence under magnetic enhancement is similar to the case where no magnets were used (see Figure 6 and Figure 7). However, the discharge current is much higher, as expected, under magnetic enhancement. Discharge currents as high as 1.3 A were obtained compared to a maximum of 0.27 A without the magnets (see Figure 7). This enhancement is important since the number density of extracted ions from the discharge (ion current) is directly related to the plasma density in the discharge chamber. Ion current as high as 50 μA at the substrate location were obtained. Note that the ion current shown in Figure 8 was taken at a distance of ~ 10 cm from the ion source, while the substrate holder is ~ 30 cm from the source. This results in a lower ion current at the substrate location by a factor of ~ 10 . The maximum ion current (at the substrate location) obtainable from the source without magnetic enhancement was below 10 μA .

Despite the improvements made in achieving higher ion current and discharge density, the life time of the filament is still a major operational issue. At high discharge currents, ion bombardment and reaction with the filament tends to shorten the filament lifetime to only a few hours.

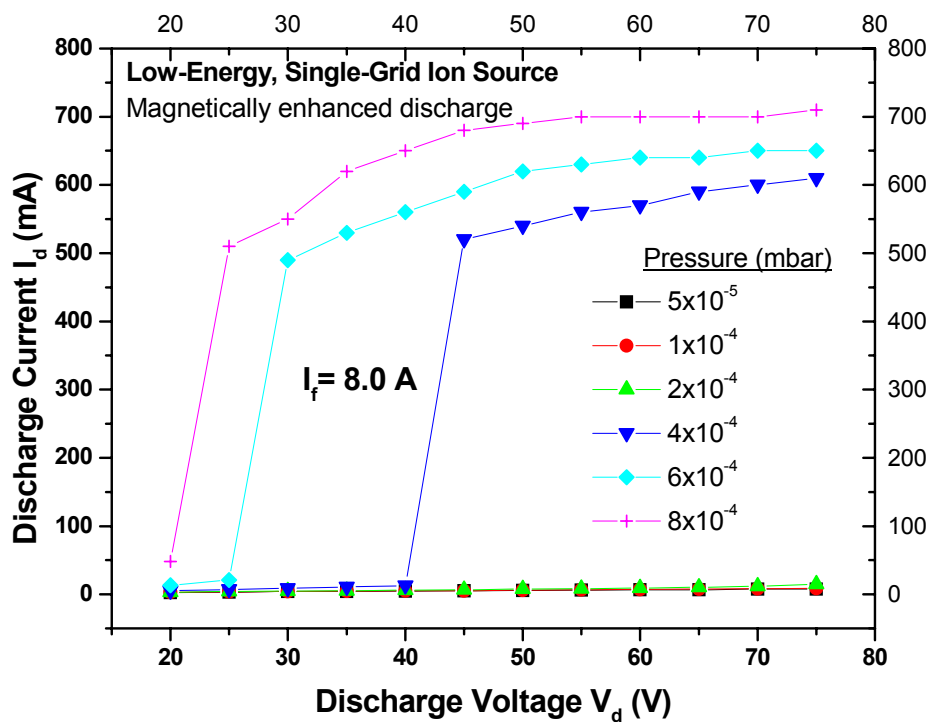


Figure 10. The dependence of the discharge current on the discharge voltage for several H_2S pressures.

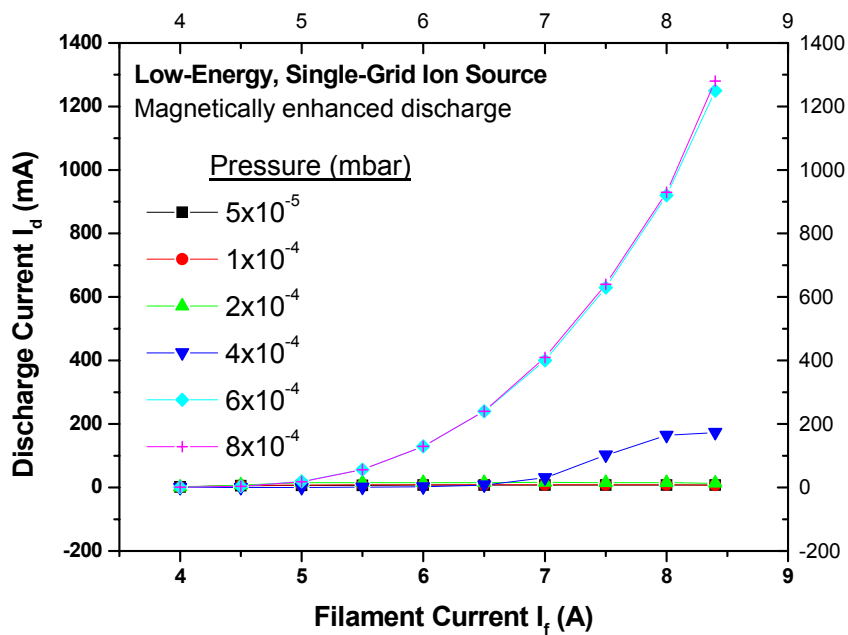


Figure 11. The dependence of discharge current on the cathode current (cathode temperature) for various discharge pressures.

3.0 Cd EVAPORATION SOURCE (EFFUSION CELL)

Cd is a high-pressure material that requires low temperature to achieve reasonable evaporation rates. The vapor pressure of Cd is equal to 10^{-2} torr at a crucible temperature of $\sim 260^\circ\text{C}$. The impingement rate, R , calculated using Maxwell-Boltzmann distribution, on a surface exposed to this vapor pressure can be estimated using the relation:

$$R = 3.513 \times 10^{22} \left(\frac{P}{\sqrt{MT}} \right) (\text{atoms.cm}^{-2}.\text{s}^{-1}) \quad (1)$$

where M is the atomic (molecular) weight in grams and T is the temperature in degree Kelvin. P is the pressure given in torr. For $P=10^{-2}$ torr, $R=1.91 \times 10^{18}$ atoms.cm $^{-2}$.s $^{-1}$. The opening of the effusion cell used for the current experiment is ~ 3.3 cm in diameter. This means that the total number of atoms, F , effusing from the cell opening toward the substrate is $R \times A$, where A is the area of the cell opening, which results in a total flux $F = 1.67 \times 10^{19}$ atoms/s for the pressure value given above.

For the CdS(100) surface, one ML of atoms corresponds to 5.88×10^{14} atoms/cm $^{-2}$. The growth rate then can be calculated by dividing F by the surface atom density. A geometrical factor related to the distance between the cell opening and the substrate position must also be taken into account. The geometrical factor, which can be approximated by the cosine law, results in a further reduction in the net deposition by $(\cos^2\theta/\pi r^2)$, where r is the distance between the cell and the substrate, and θ is the angle between the cell axis and the substrate location. In our MBE system, $r \cong 40$ cm and $\theta = 0$. This results in an estimated net deposition of ~ 5.7 ML/s for cell operating temperature of 260°C . This rate is more than needed in typical operating conditions, which ranges from one to two ML/s.

In summary, Cd is a high vapor pressure material that requires a rather low temperature ($<300^\circ\text{C}$) to achieve the needed evaporation rate. For this reason, we have decided to build our evaporation source with a maximum possible temperature of $<400^\circ\text{C}$. This is important in order to avoid accidental release of large quantities of Cd into the system. Most commercial effusion cells are designed to operate at high temperatures (typically above $\sim 500^\circ\text{C}$). An inadvertent mistake of operating the cell at high temperatures would overflow the system with Cd.

A schematic drawing for the new cell is shown in Figure 12. The crucible is made of quartz that is welded to a 2.75 inch stainless steel flange. The quartz/steel junction can withstand repeated bakeout to 400°C and usable to below 10^{-11} Torr. The cell is fitted to one of the eight 4.5 inch ports designed to accommodate various evaporation sources. A high impact fiberglass cylinder is mounted on the 4.5 inch flange and acts as a protection shield to the quartz tube. A cylindrical metal integrator is mounted on top of the cell and extends toward the substrate to shield the system from excessive deposition of Cd. The shield can be removed and replaced as needed. The Cd charge is heated resistively by a heating mat assembled to the outer surface of the quartz tube. This design has the advantage of separating the heating elements from the vacuum system. The heating elements can be serviced and replaced without venting the UHV system. In addition,

unnecessary degassing and contamination generated by the heater and its shields can be avoided. A thermocouple is attached to the crucible and connected to a digital readout device. The resistive heater and the thermocouple assembly are shielded by a stainless steel foil in order to reflect the heat toward the cell. A proportional temperature controller with a set point is used to control the temperature in the cell. The controller provides the cell with a high degree of temperature stability.

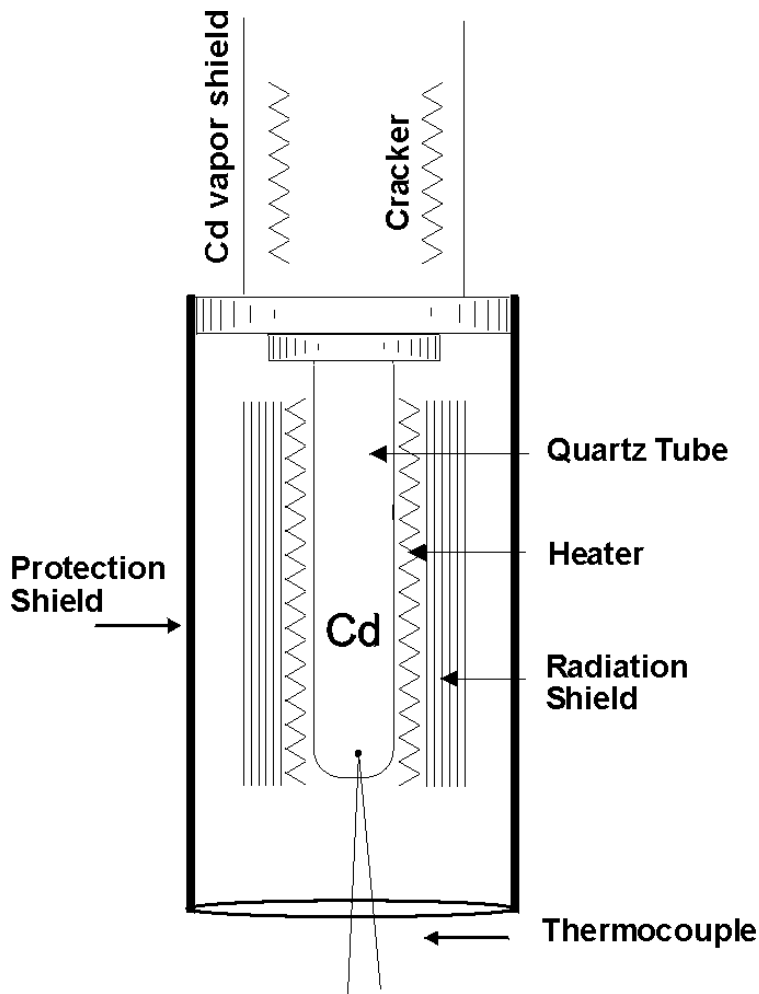


Figure 12. A schematic showing the Cd effusion cell.

3.1 Monitoring and Calibration of the Cd Flux

We have attempted to determine the dependence of the deposition rate on the Cd cell-temperature. A Si wafer was used as a substrate. The wafer was wrapped by three thin metal strips, as shown in Figure 13. The metal strips shield a fraction of the wafer from deposition, which results in the formation of thin film steps at the edges of the metal strips. Measuring the

step height then provides the thickness of the deposited films. This arrangement of the metal strips is intended to give a detailed mapping of the deposition rate versus position on the wafer.

Deposition of Cd was carried out on the Si substrate described above, but no deposition was observed on the Si sample. The cell temperature was increased to 350 °C to ensure a high deposition rate of Cd, while the substrate was kept at room temperature in order to enhance the sticking probability of Cd on Si. No measurable deposition was observed on the Si surface. However, a rather thick layer of Cd was deposited on most of the metal shield mounted on the effusion cell (see Figure 12) except for the smooth portion of the metal shield. This clearly demonstrates that a high flux of Cd was supplied by the effusion cell to the substrate, but no deposition took place due to extremely low sticking probability of Cd on Si. This result is not surprising since the low sticking probability of Cd is well documented in the literature.

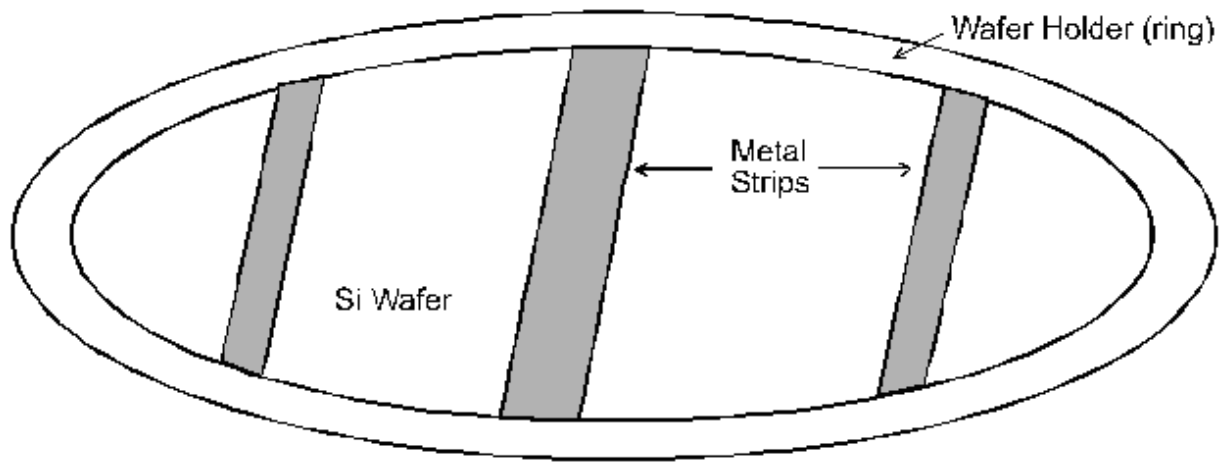


Figure 13. Schematic showing the wafer assembly used for calibration of the deposition rate from the Cd effusion cell.

Since the absolute value of the deposition rate cannot be measured using conventional methods, we attempted to monitor the rate using other alternatives. These methods are based on mounting a movable sensor that can be moved into the beam path between the vapor source and the substrate (see Figure 14). Alternative monitoring methods can be summarized as follows:

1. Mount a movable ion gauge that can be moved in front of the substrate or to a location equivalent to the substrate position with respect to the effusion cell. The ion gauge measures the pressure of the Cd beam which is related to the deposition rate by Equation (2):

$$R = 3.513 \times 10^{22} \left(\frac{P}{\sqrt{MT}} \right) (\text{atoms.cm}^{-2}.\text{s}^{-1}). \quad (2)$$

This method is rather common for materials with low sticking probability.

2. Use an electron impact emission spectroscopy (EIES) sensor. This sensor contains a shielded anode and cathode with a rectangular orifice between the two electrodes. When the vapor of a material passes through the orifice, it becomes partially ionized or excited by electrons emitted from the cathode and accelerated toward the anode. Excited atoms then relax to the ground state emitting a photon with an energy related to the type of the atoms in the beam. A photomultiplier

is then used to measure the intensity of the emitted light, which is related to the deposition rate. This sensor is reliable and has a long life time. However, it requires a frequent calibration to ensure correct measurements. This alternative is expensive, but we had the power supply for the unit.

3. Mass spectrometer. A mass spectrometer would be a reliable alternative for rate measurement through measuring the partial pressure of the deposited atoms.

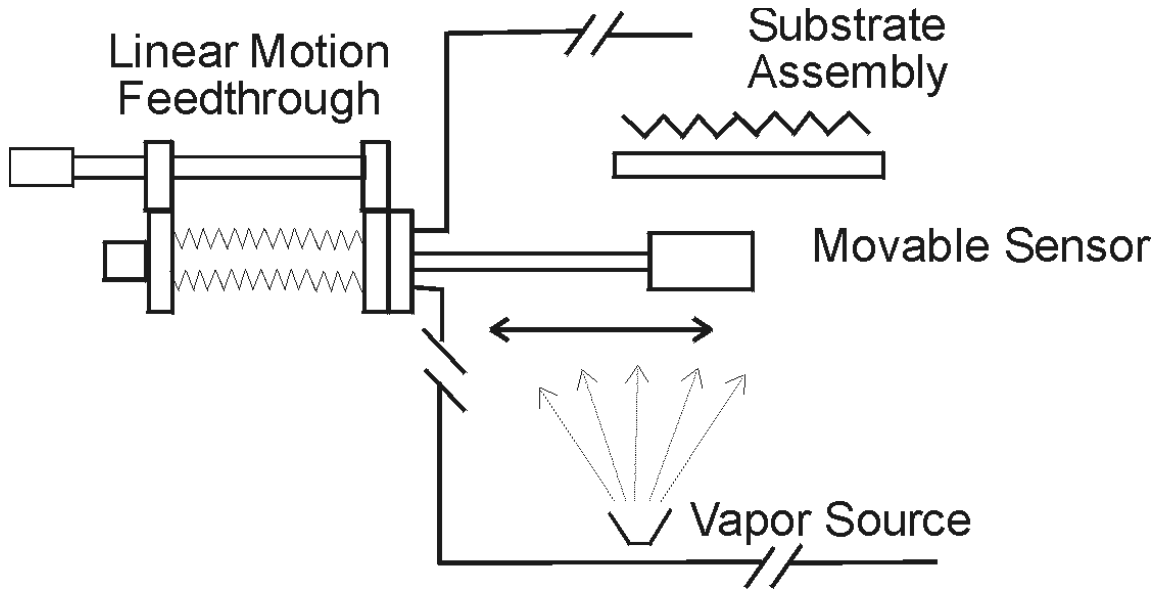


Figure 14. A schematic showing the setup needed for mounting a sensor to measure the deposition rate of Cd at the sample location

Among these possibilities, we have selected the first option, a movable ion gauge. This option is easier to service, can be mounted to our MBE system with no major modifications, and more economical.

3.2 Construction of a Movable Ion Gauge for Monitoring Cd Flux

The easiest and most economical alternative to monitor the Cd flux (also usable for sulfur flux) that fits the MBE system without major modification is the use of an ion gauge. As explained above (see Figure 14), the ion gauge must be movable to a location between the sample and the vapor source (effusion cell) in order to measure the vapor pressure of the incident Cd flux, which is proportional to the deposition rate, as given by Equation 2. We have designed and constructed a movable gauge that can be mounted to one of the eight ports on the source flange of our MBE system (see Figure 3). The details of the design are shown in Figure 15. A rotary feedthrough, mounted to a custom-made tube via a 1.33 inch Conflat[®] flange, controls the movement of the ion gauge. The feedthrough rotates a pinion, which in turn moves the rack linearly along the assembly axis. The custom-made tube ends on one side by a 4.5 inch flange while the other end is

welded to a 2.75 inch flange. The T-section at the end of the tube (see Figure 15) provides a feedthrough for the ion gauge wires, a window, and an extension space for the movement of the rack.

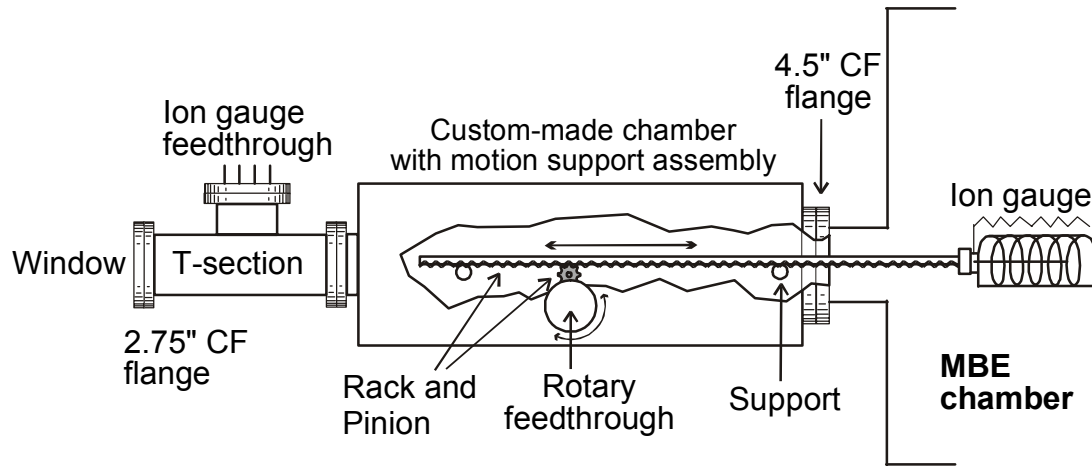


Figure 15. A schematic of the movable ion gauge

4.0 DESIGN AND CONSTRUCTION OF A COMPACT, INDEPENDENTLY PUMPED

EVAPORATION SOURCE FOR LA

We have made three design alternatives for La evaporation using (1) RF heating, (2) resistive heating, and (3) combined resistive and electron-beam heating. La is sensitive to oxygen and moisture and must be handled under dry atmosphere. Originally, we proposed to use an electron beam evaporator (EBE) fitted with a shower of Ar (or N₂) on the La charge so that the La would be flooded with Ar during system service and repair. However, it is more practical to design a compact evaporation cell that can be isolated from the system and kept under vacuum during system repair and service. This design will also allow removal of the cell from the system while under vacuum for recharging with La in a glove box. A schematic showing the details of the source is shown in Figure 16. All three alternatives share the same basic source design except for the heating elements. The whole cell assembly is mounted on a linear translator capable of 8 inch linear travel. The linear translator can move the crucible assembly between the MBE chamber and the source housing. The source housing can be isolated from the MBE chamber by a gate valve. Before venting/servicing the MBE system, the gate valve can be closed, which protects the La source from atmospheric pressure. When the La evaporation source needs service, the whole assembly (linear translator, source housing, and valve) can be isolated from the MBE chamber and moved into a glove box for service. The heating assemblies were different in the three alternatives mentioned above. In the following, a brief description is given for each assembly.

(1) RF heating: In this case, the heater is a water cooled coil connected to a RF power supply through a feedthrough, and the crucible is made pyrolytic boron nitride (PBN). We have completed this design and built a matching network between the power supply and the coil to match the load impedance to the impedance of the power supply in order to deliver maximum power to the La charge and minimize the reflected power. We have pursued this approach and were close to matching the power supply to the load. However, a failure in the RF power supply demanded repair or replacement of the unit, which was beyond the allocated budget. As an alternative, we have changed the design as described below.

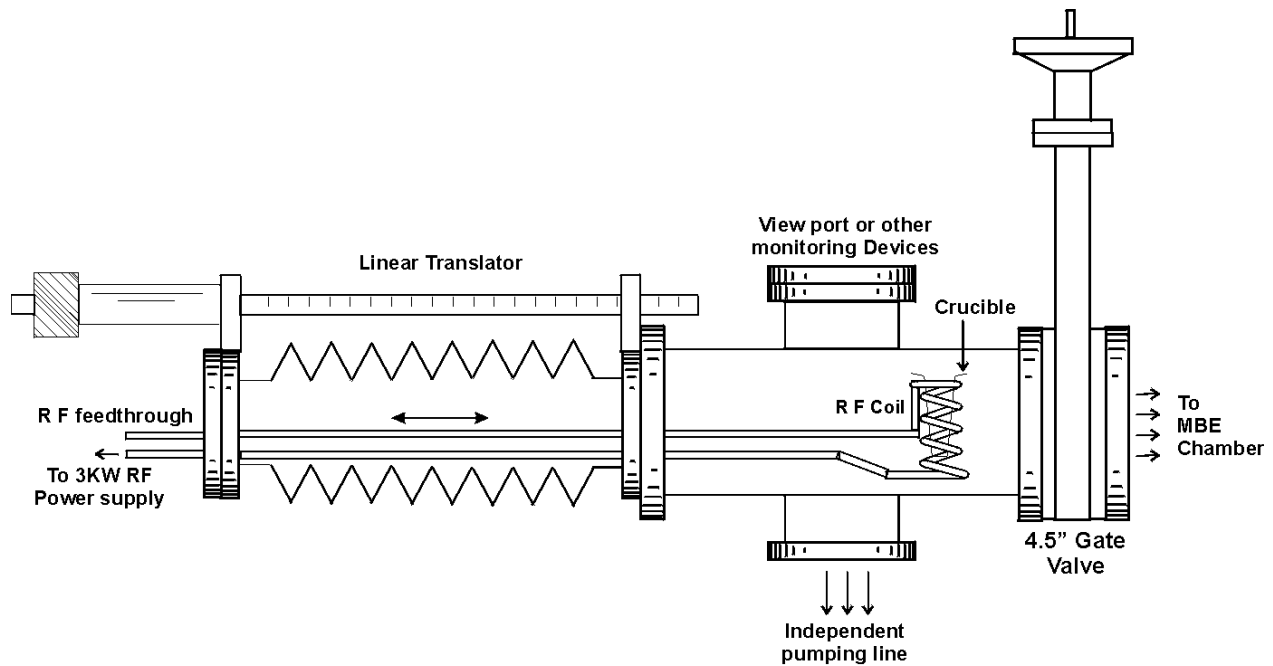


Figure 16. A schematic showing the design of the RF source

(2) In this approach, the RF heater assembly was replaced by a tungsten (W) resistive heater in which current is passed directly through the W wire to heat the crucible. The crucible was made of PBN similar to the case of RF heating. This approach was rather acceptable. However, the demands of reaching a temperature over 1300 °C in the crucible necessitate the use of high heating current. This, in turn, resulted in short filament life time. Since the service of the cell must be carried out in a controlled-atmosphere glove-box, the repair of the cell was cumbersome and expensive. The whole cell assembly had to be gated (gate valve closed), removed from the MBE system, loaded into the ante-chamber of the glove box, pumped down, and finally moved into the glove box and then serviced. Due to the detailed and miniature nature of the heater assembly, the repair had to be carried out in air. In order to minimize the repair cycle, the heater assembly was modified as described in (3) below.

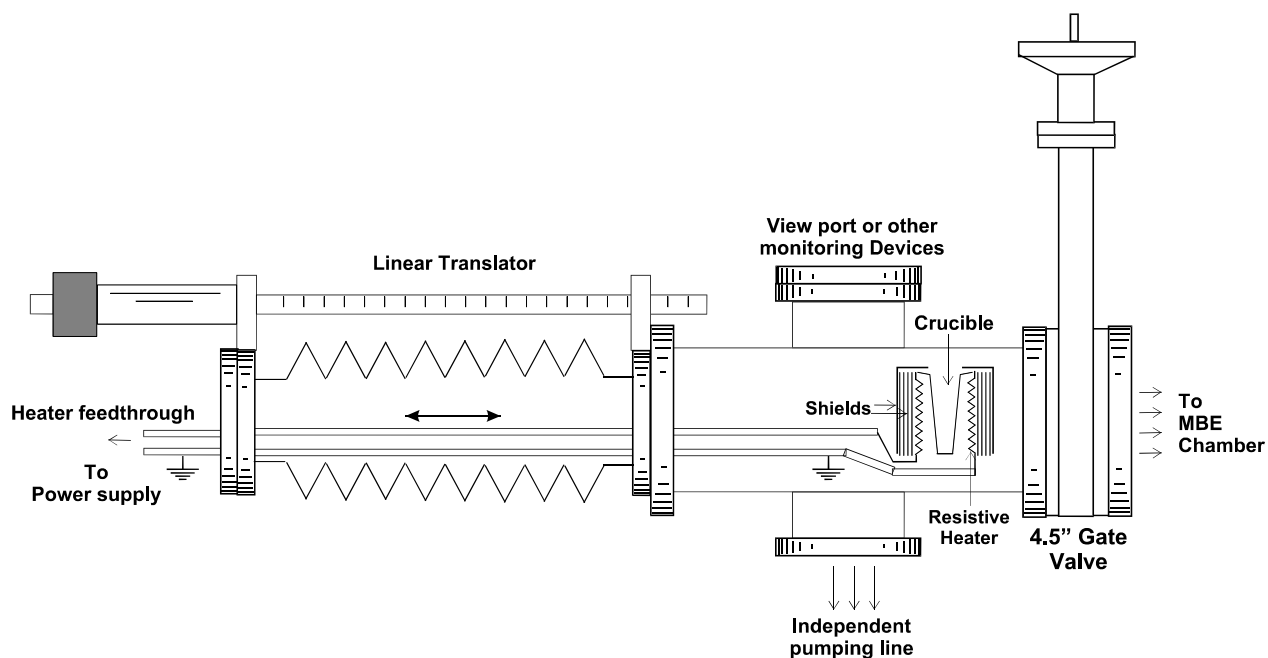


Figure 17. The La source fitted with resistive W heater

(3) To reduce the demands of high currents in the W heater, electron beam heating was utilized in the following way: the PBN crucible was replaced by a Ta crucible (conducting) and bias was either applied to the crucible or the heater. As a result of bias application, electrons emitted from the W filament are accelerated toward the crucible, resulting in electron irradiation of the crucible and thus heating. Ta was chosen since it has very low vapor pressure and has no reported reactivity with La.

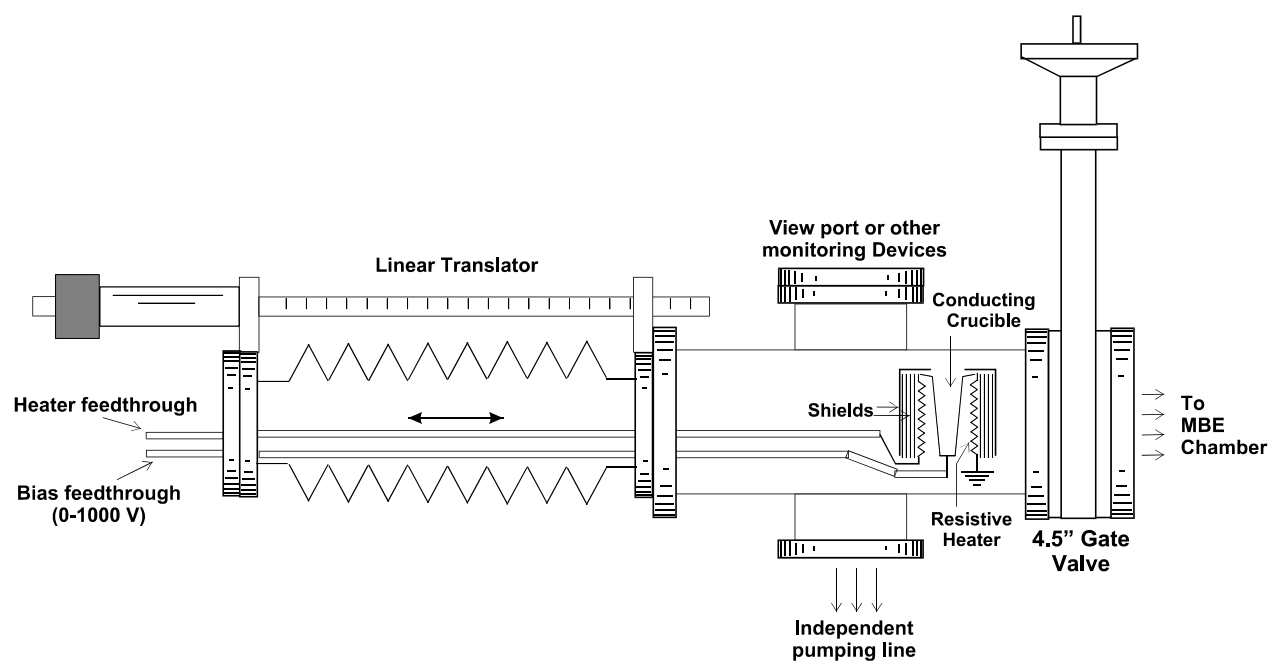


Figure 18. The La source fitted with conducting crucible made of Ta in which the crucible or the heater is biased (0-1000V) to facilitate electron irradiation of the crucible resulting in high cell temperature

PART 2: GROWTH AND DEVICE FABRICATION

5.0 ION-ASSISTED DEPOSITION USING SINGLE-GRID ION SOURCE

5.1 Initial Experiments: Deposition on Si(100)

Deposition of CdS was carried out using the system configuration described in Part 1. The ion source was used without magnetic enhancement. Initial experiments were carried out on Si wafers. The Si wafer was cleaned insitu using thermal desorption of the surface oxide layer by annealing the sample at 850 °C. Deposition was carried out using Cd cell temperature of 250 °C and a sulfur/hydrogen ion current of $\sim 1 \mu\text{A}/\text{cm}^2$ at the substrate position. The ion energy used was 700 eV. The deposition time was 6 hours and the substrate temperature was 150 °C. The sample was analyzed by MCNC for Auger depth profile analysis and AFM as well as scanning electron microscopy (SEM).

Figure 19 shows an AES depth profile from a sample grown under the conditions described above. The figure shows the measured AES signals of Si, S, Cd, and O versus the depth in the sample. The sample seems to be close to stoichiometric CdS but slightly rich in sulfur. The slight deviation is most likely an artifact of AES analysis, but could be due to the high ion energy (700 eV) used during deposition and low Cd deposition rate. The high ion energy can result in enhanced incorporation of S in the film as well as shallow S implantation. On the other hand, high energy S ions may sputter the grown layer resulting in an effective low growth rate. The atomic concentration as determined from the survey of the whole spectrum is shown in Table 2. The values in the table, while still approximate, are in general more accurate than the values given in the AES depth profile shown in Figure 19. This is due to a different method of data acquisition. A survey scan is comprised of 10 sweeps of the spectrum, while the depth profile data are calculated from 3 to 6 sweeps of the specific peaks in order to minimize data acquisition time. The sample thickness, calculated from the depth profile, is ~ 12 nm which indicates a low deposition rate at the current growth conditions. The measurable O signal at the interface is due to residual silicon dioxide on the Si surface prior to growth.

Individual AES scans over a wide energy range were also taken from the surface of the sample (as received) and after sputtering for 1 sec (within the sample thickness). The AES spectra are shown in Figure 20. The spectrum from the as received sample surface (Figure 20a) show mainly Cd and S with a minor O signal. No signal from other materials can be observed. This result indicates that the CdS surface is rather inert to oxidation and other contamination. The sample was left in air for more than a week between growth and analysis. Despite the long exposure to atmosphere, the O signal is low and represents less than 1.5 percent of the surface composition.

The spectrum taken after sputtering for 1 second (Figure 20b) shows no evidence of measurable contamination signal, which indicates that the deposition environment was free of contamination.

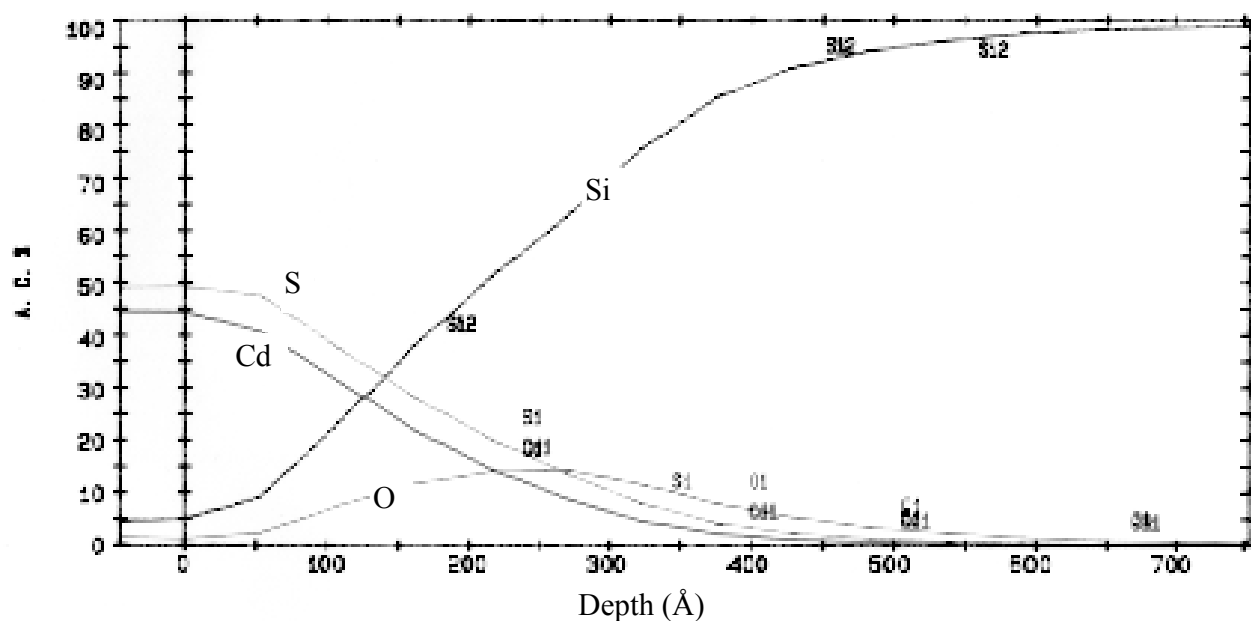


Figure 19. AES depth profile of the CdS layer grown on Si(100) under the conditions described in the text.

Table 2. Auger analysis of the CdS film.

Element	As received	after 1 sec sputter
Si	0.00	0.00
S	56.93	57.89
Cd	41.37	41.40

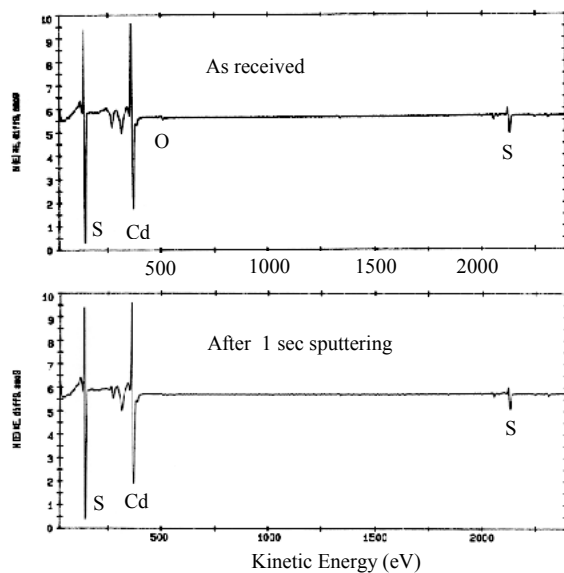


Figure 20. AES spectra from the surface of the sample as received (a) and after sputtering for 1 second (b)

The sample surface is rather homogeneous with no major features. An SEM image of the surface is shown in Figure 21. However, AFM studies show a surface roughness on the nanoscale. It is possible that the surface roughness is induced by ion bombardment.

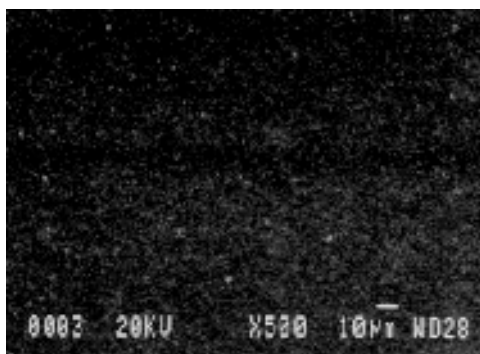


Figure 21 SEM image taken from the same sample

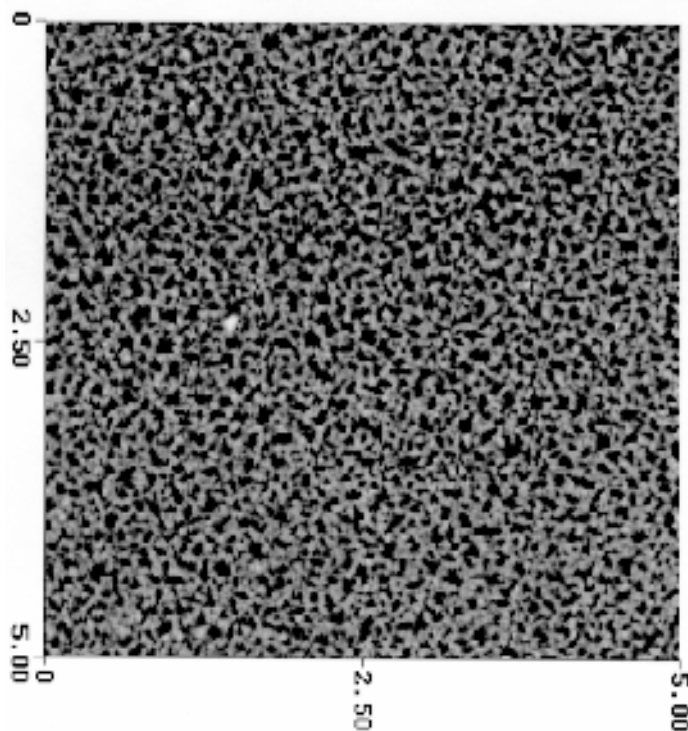


Figure 22. AFM image from the same sample taken from a 5 µm by 5 µm area

5.2 Problems and Challenges Associated With the Use of Ion-Assisted Deposition

The major problems encountered in these initial experiments can be summarized as follows:

Low deposition rates: This problem could be related to two factors:

1. Low number density of ionized S atoms provided by the ion source during the growth.
2. Low sticking probability of both Cd and S on the substrate resulting in a low Cd-S incorporation rate at the growing surface.

The effective deposition rate was as low as ~ 2 nm/h.

Reliability of the ion source during growth: since the fraction of ionized sulfur atoms plays a crucial role in achieving reasonable deposition rate, the ion source had to be operated at its maximum limits. This translates into high discharge current, high filament current, high discharge voltage, and high acceleration voltage (see Part 1 for description of the ion source and its operation). These conditions result in an accelerated filament failure, sparking, and electrical shortages between various parts of the ion source. Since the growth rate is very low, growth of useful CdS layers requires many hours of continuous operation of the ion source under extreme conditions. This has led to frequent failures of the ion source during growth. Servicing the ion source requires venting the MBE system, which has caused long delays and unwanted exposure of the MBE system to atmosphere. These problems can be partially remedied by changing the design of the ion source. However, such an operation, while durable, would come at the cost of achieving our main goals in growing CdS and LaS layers within the time frame set for the project.

For these reasons, we have utilized an RF atomic source as an alternative to the ion source. The RF source utilizes RF power to generate plasma, which eliminates the needs for the filament and can generate much more intense plasma.

6.0 DEPOSITION OF CdS USING RF ATOMIC SOURCE

Highlights:

Cubic CdS was grown over wide range of temperatures (100 to 500 °C) as demonstrated by in-situ RHEED measurements.

Stoichiometric CdS was deposited on InP(100) substrates. Much higher deposition rates were achieved and a reliable, reproducible method of deposition was developed.

Failure of experiments due to needs for service was minimized. For the whole duration of the project, the RF source was serviced only twice.

A rather smooth CdS surface was obtained (roughness in the range of 1.5 nm), indicating the formation of continuous layers and the absence of island growth mode.

The CdS/InP interface is atomically abrupt with no indication of interdiffusion between the grown layer and the substrate, as indicated by transmission electron microscopy (TEM) and AES depth profiles.

6.1 The RF atomic source

Figure 23 shows a schematic for the RF source used in the current experiments. The source consists of three main components: RF coil, controlled gas delivery line, and a plasma chamber. The gas, in this case H_2S , is fed to the discharge chamber through a precision leak valve connected to the gas-inlet flange. The plasma chamber is made of PBN tube, a high temperature insulating material. The PBN tube is mounted on the gas-inlet tube, which is made of stainless steel, and capped by a small orifice in order to enhance the pressure difference between the PBN tube and the vacuum chamber. In this way the pressure inside the PBN tube can be more than one order of magnitude higher than the pressure in the vicinity of the sample. This condition is necessary to generate intense plasma in the tube at a low operating pressure. The RF power is supplied through a water-cooled copper tube formed into a coil around the plasma chamber.

The RF power induces intense plasma in the PBN tube, which results in dissociation of H_2S into H and S ions. These ions effuse through the orifice and may recombine with electrons to form a neutral atomic beam. The intensity of the plasma, as well as the emitted photon spectrum, can be monitored through the view port. We have measured the spectrum dependence on the plasma operating conditions using the setup shown in Figure 24. The setup consists of a fiber-optic cable connecting the view port on the RF source to a monochromator (spectrometer). The intensity of the emitted light spectrum is then measured by a photodiode mounted at the exit slot of the monochromator. A digital oscilloscope then amplifies the photodiode signal while LabView (a control software operating on IEEE488 card) records the spectrum. The spectrometer, which was made by Oriel, has a usable wavelength range from 180 to 1000 nm.

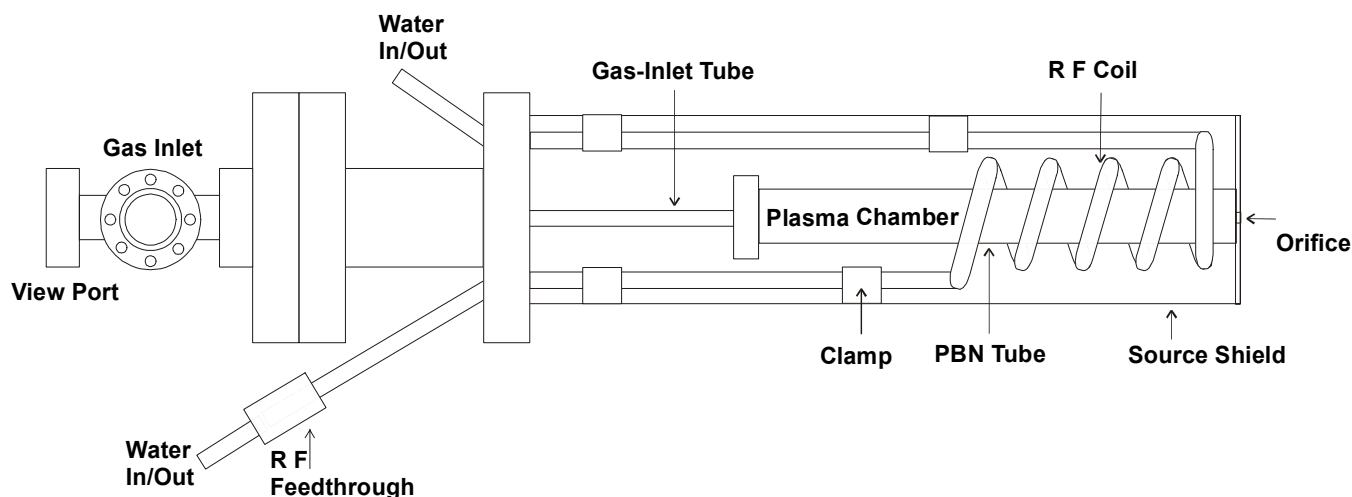


Figure 23. A schematic of the RF source used in the current experiments

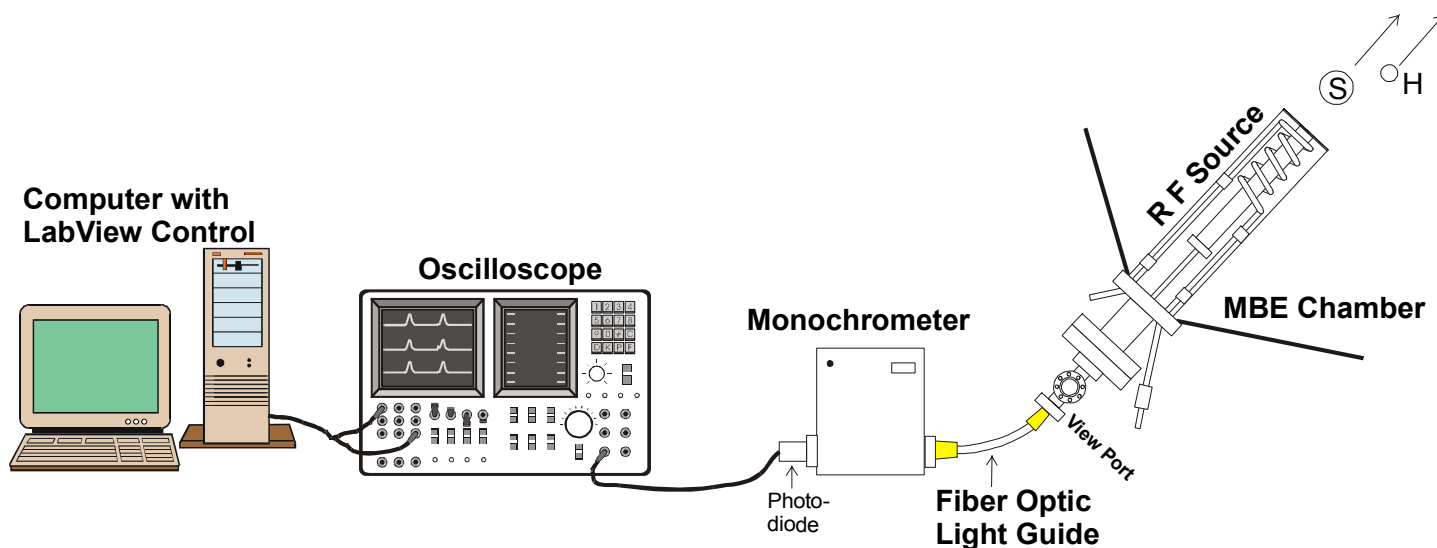


Figure 24. The experimental setup used for spectra measurements from the RF source

Typical spectra from operating the RF source using H_2S gas are shown in Figure 25. The figure shows spectra for three RF power settings, 200, 300, and 400 W. Each peak in the spectrum is related to emission from a specific atom or a molecule. The two major peaks in the spectrum are related to atomic hydrogen ($\lambda = 658 \text{ nm}$) and atomic sulfur ($\lambda = 930.5 \text{ nm}$). These values are close to those reported in the literature, 656.3 nm for H and 923.7 nm [32]. The small difference is most likely related to a possible experimental error in calibrating the spectrometers in various laboratories, since the reported values were measured in the late 1960s. The other peaks, around

950 nm and 870 nm, are attributed to S molecules (S_x) or possibly to S_x -H complexes forming due to the presence of reactive S atoms.

These results clearly demonstrate the presence of atomic-S, which is a prerequisite for CdS growth. Figure 25 also shows that the concentration of S atoms, which is related to the peak intensity, is proportional to the RF power, as expected. The relationship between the RF power and the atomic-sulfur peak intensity is plotted in Figure 25 for RF powers ranging from 200 to 400 W. Results are shown for two gas pressure values, 5×10^{-4} and 1×10^{-3} mbar, respectively. The fraction of atomic-S in the plasma increases with increasing power and H_2S gas pressure.

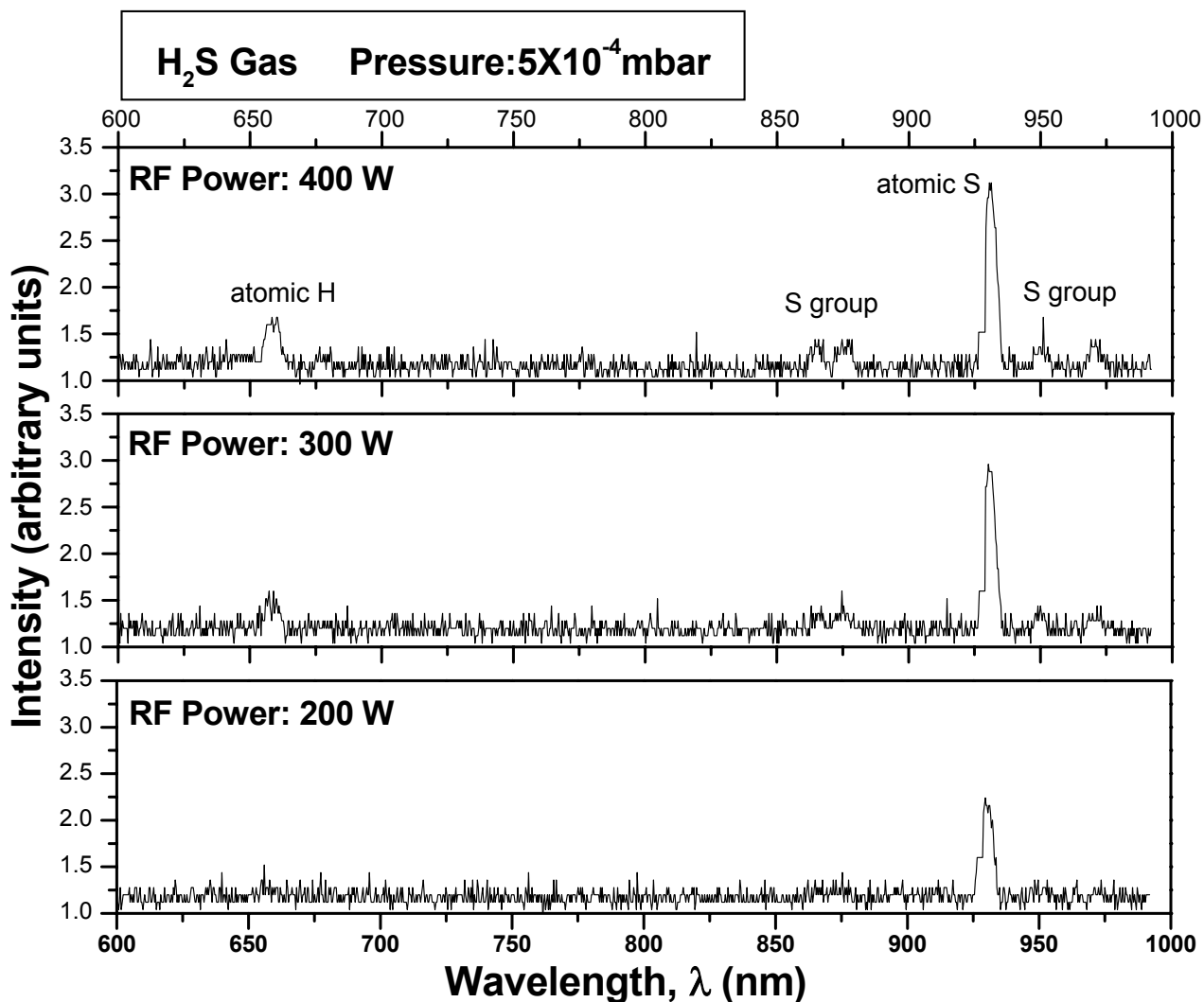


Figure 25. Typical spectra from the RF atomic source

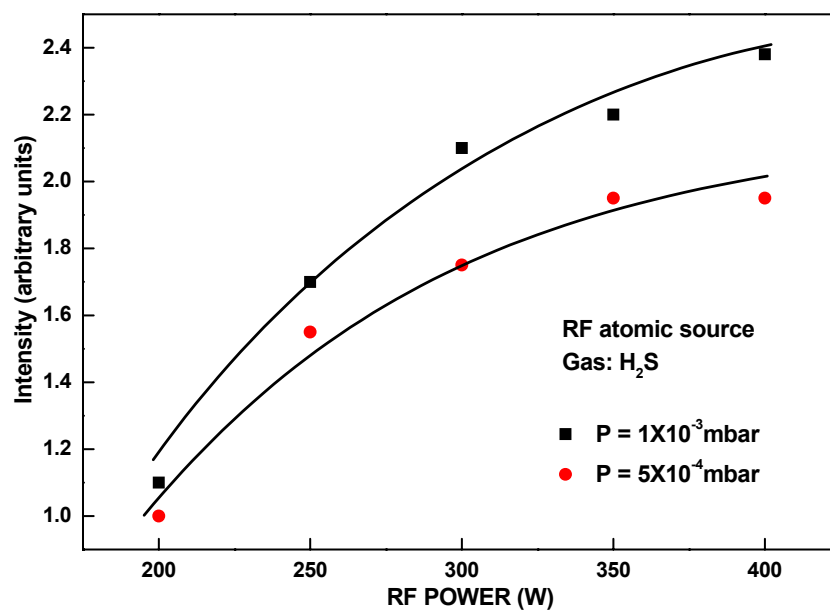


Figure 26. The dependence of the atomic S peak-intensity, which is related to the atomic S concentration, on the RF power for two H_2S gas pressures

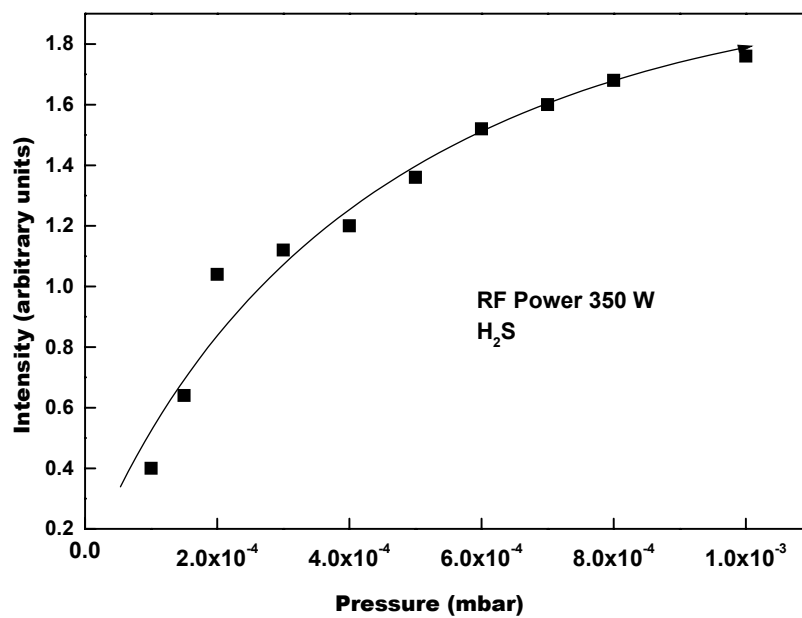


Figure 27. The dependence of S atomic fraction on the gas pressure at a RF power of 350 W

The relation between the S atomic fraction and H_2S gas pressure is further exemplified in Figure 27. At low pressures, the S atomic fraction increases linearly with increasing pressure while a slower proportionality was obtained at high-pressure values. We are currently working to establish the effects of gas pressure, RF power, and substrate temperature on the growth rate and the quality of the grown CdS layers.

6.2 Deposition of CdS on InP(100) Substrates

CdS layers grown using the RF atomic source and a Cd effusion cell are cubic as indicated by RHEED observations. Typical RHEED pattern obtained from a clean InP(100)2x1 surface is shown in Figure 28(a). The 2x1 reconstruction indicates that the surface is clean, while the streaky nature of the pattern indicates that the surface is smooth. In Figure 28(b), the diffraction pattern from CdS is shown. The pattern demonstrate growth of cubic CdS. No other phases or crystal orientations can be seen in the pattern. The streaks indicate that the CdS surface is smooth. The InP surface cleaning was conducted by exposure to atomic flux from the H_2S atomic source at 400 °C. Our experiments have shown that this procedure is much better than thermal cleaning. In thermal cleaning, the sample is heated to ~ 550 °C, which results in an indium (In)-rich surface due to evaporation of phosphorous (P) from the InP surface. The diffraction pattern resulting from thermal cleaning is also inferior to the one observed after H_2S exposure.

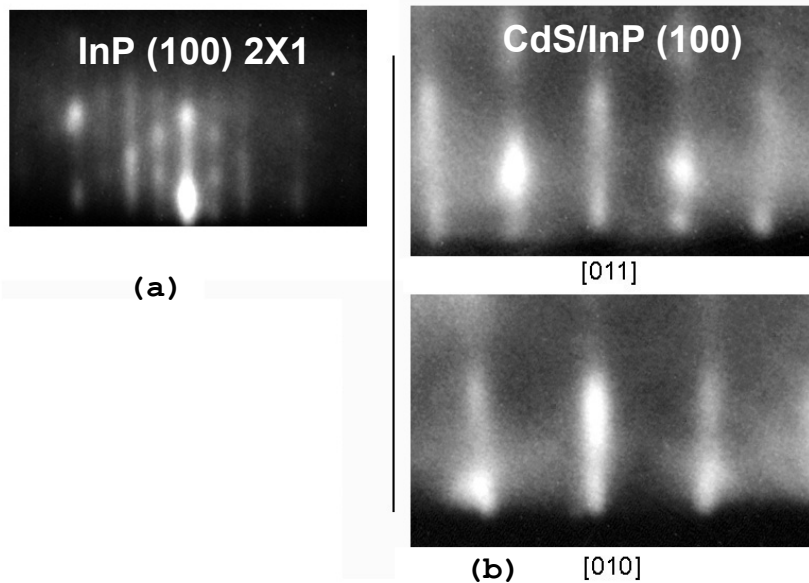


Figure 28. RHEED pattern taken from (a) clean InP(100)2x1 and (b) after growth of CdS

Figure 29 shows a typical AES depth profile, taken from a CdS layer grown at substrate temperature $T_s = 150$ °C using the RF atomic source to supply S atoms and an effusion cell for the Cd beam. The atomic concentrations, calculated from an AES depth profile, indicate a stoichiometric CdS composition. The depth profile also demonstrates that the CdS/InP interface is abrupt and there is no interdiffusion between the layer (CdS) and the InP substrates. Moreover, no measurable contamination signals were obtained during the survey measurements.

The surface roughness of the grown samples was measured using AFM. The samples are extremely reflective and show an average roughness below ~ 2 nm. An example of such a measurement is shown in Figure 30. The sample has a mean roughness of ~ 1.13 nm over the scanned area of 8 by 8 μm^2 despite the high growth temperature ($T_s = 350^\circ\text{C}$) used for this sample.

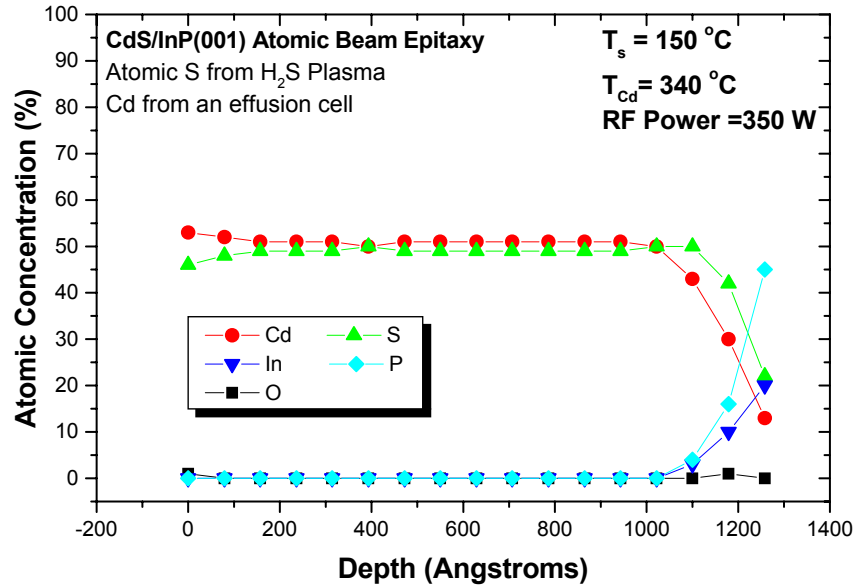


Figure 29. AES depth profile from a CdS layer grown on InP(001) substrate at $T_s = 150^\circ\text{C}$

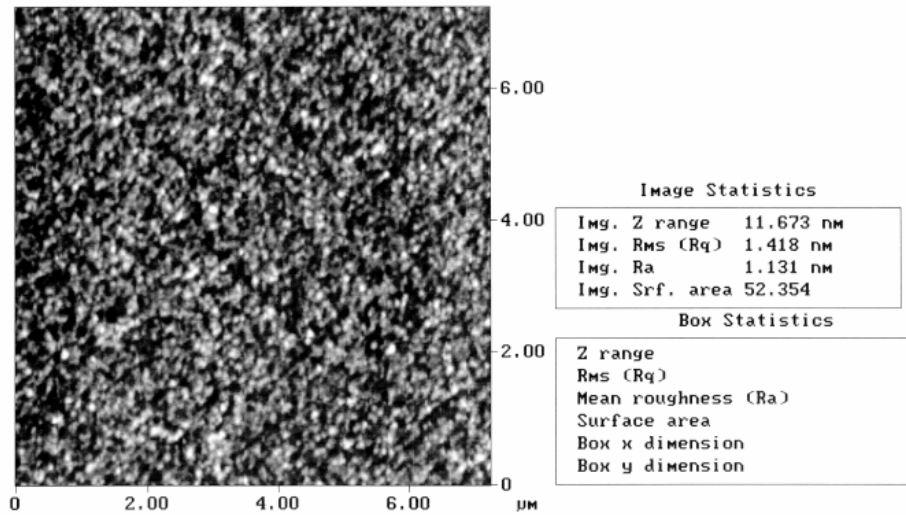


Figure 30. AFM image over 8x8 μm^2 taken from a CdS layer grown at $T_s = 350^\circ\text{C}$

CdS growth rates dependence on the Cd effusion cell temperature, measured from a set of samples grown at 150 °C and gas pressure of $\sim 1 \times 10^{-3}$ mbar, is shown in Figure 31. The RF power was set to 350 W for these experiments. The exponential dependence indicates that growth rate is proportional to the Cd pressure since the Cd pressure depends exponentially on the Cd cell temperature. The proportion also indicates that enough atomic S is generated by the RF source for the Cd-S reaction to be sustained, forming the CdS layer. It is anticipated that the growth rate will reach a steady state with increasing Cd flux if the supply of atomic S is kept constant.

Initial results on the dependence of deposition rate (R) on the growth temperature (T_s) showed an increase in R with increasing T_s . This is due to enhanced Cd-S surface reaction rate with increasing growth temperature, T_s .

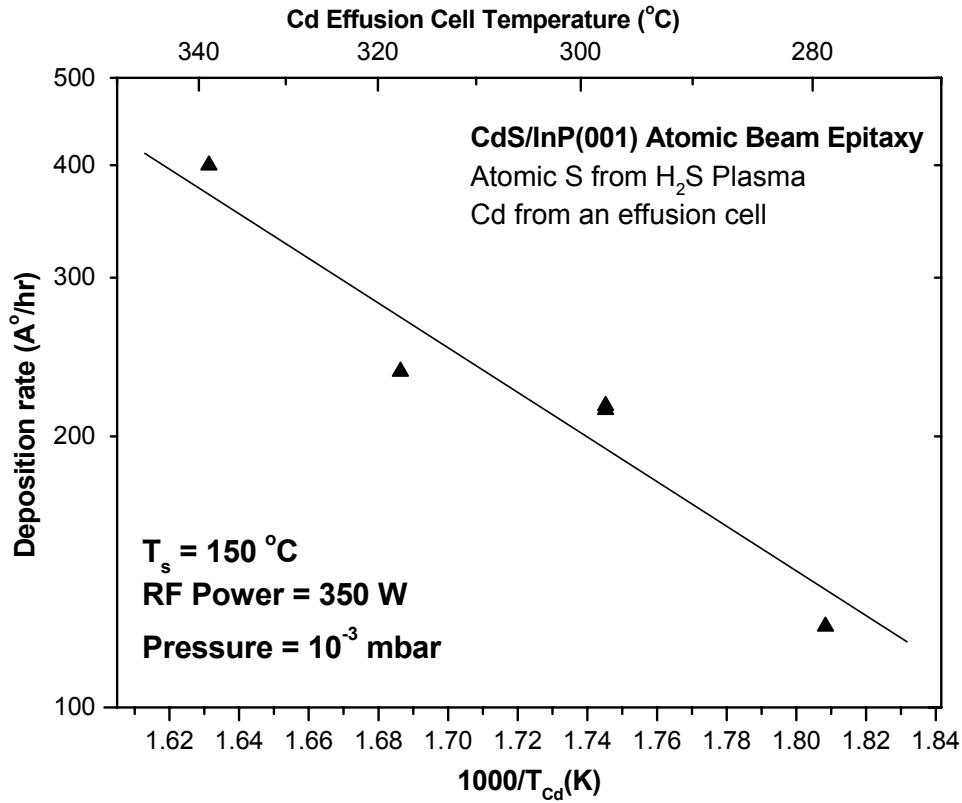


Figure 31. The dependence of growth rate on the Cd cell temperature in the figure

6.2.1 Surface Roughness of Grown Layers

Since the CdS/LaS interface and CdS layer growth mode play an important role in the performance and the capability to fabricate a successful non-thermionic field emitter device, we have examined the surface morphology of the grown layers using AFM. AFM can determine whether the layer is continuous or consists of islands as well as the degree of surface smoothness. These measurements have shown that all layers grown so far followed a layer-by-layer growth mode with no indication of island formation, which is a necessary condition for the fabrication of

the field emitter device as discussed in our proposal. Moreover, the average surface roughness, calculated from area scans of 5 by 5, 8 by 8 μm^2 , or 14 by 14 μm^2 , showed a small surface roughness in the range of 1 to 2 nm, which indicates the formation of a rather smooth surface. In the following, the surface roughness will be related to the growth conditions used in these experiments. Typical AFM scans are shown in Figure 32 and Figure 33.

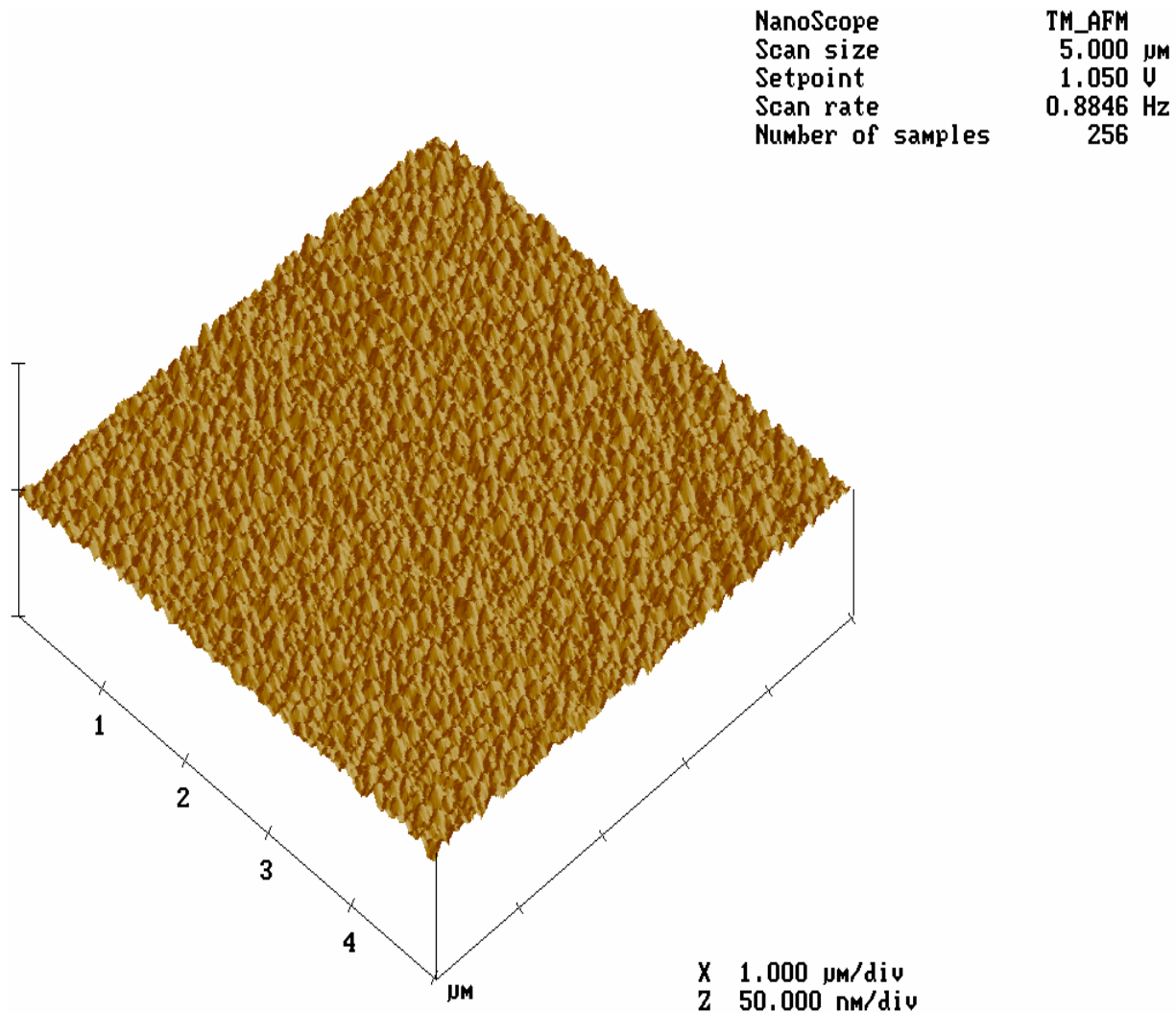


Figure 32. AFM image of a 275-Å-thick CdS layer grown at 150 °C

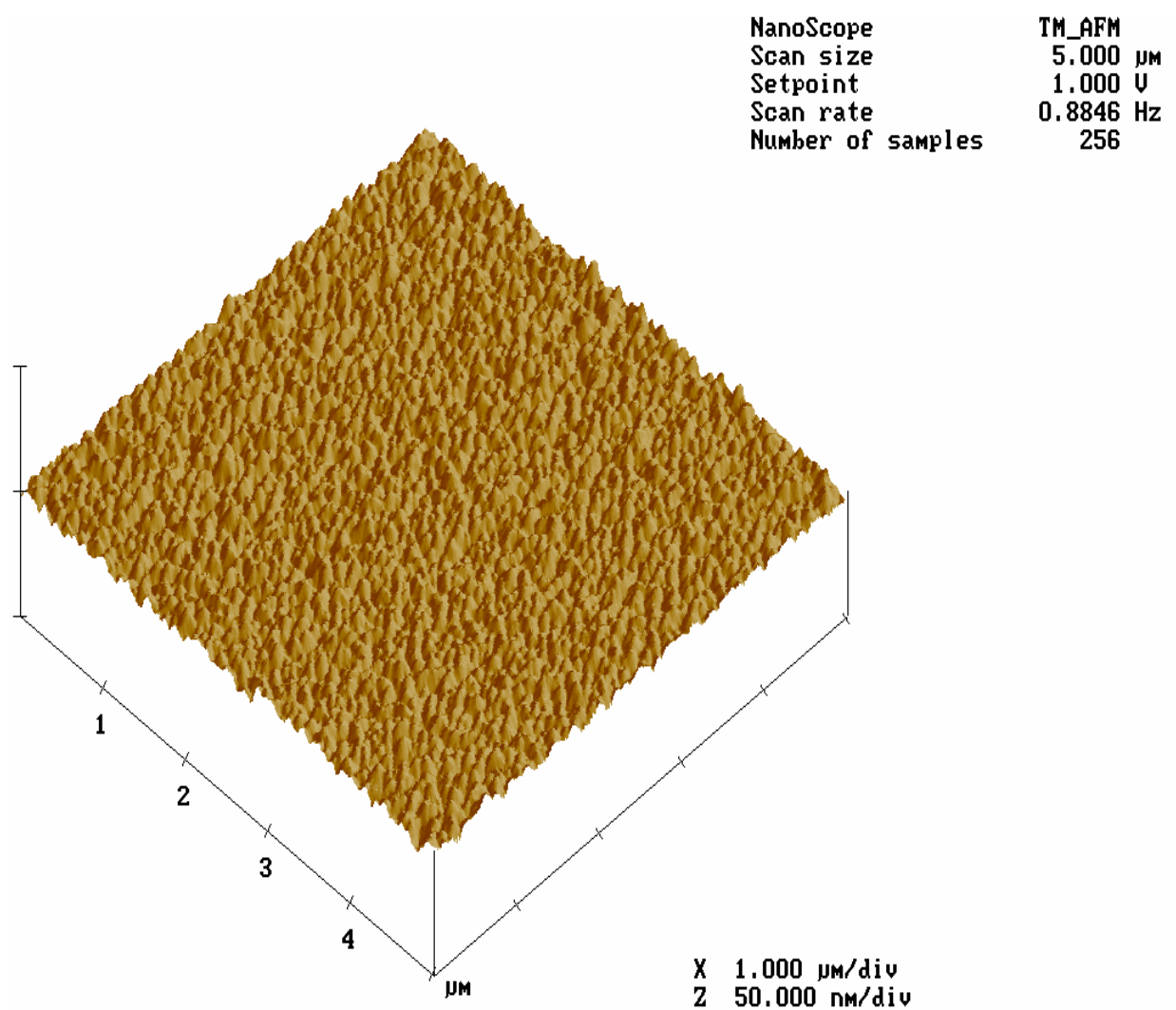


Figure 33. AFM of a 2000-Å-thick layer grown at 150 °C

In the following, the average roughness measured from AFM scans similar to those shown in Figure 32, and Figure 33, are plotted as a function of thickness, operating pressure, substrate temperature, Cd cell temperature, and RF power.

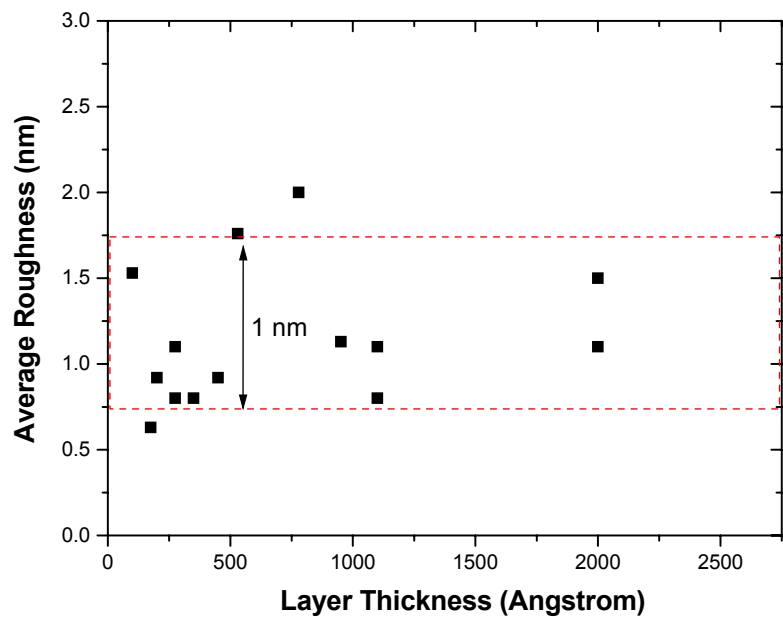


Figure 34. The average surface roughness as a function of the layer thickness

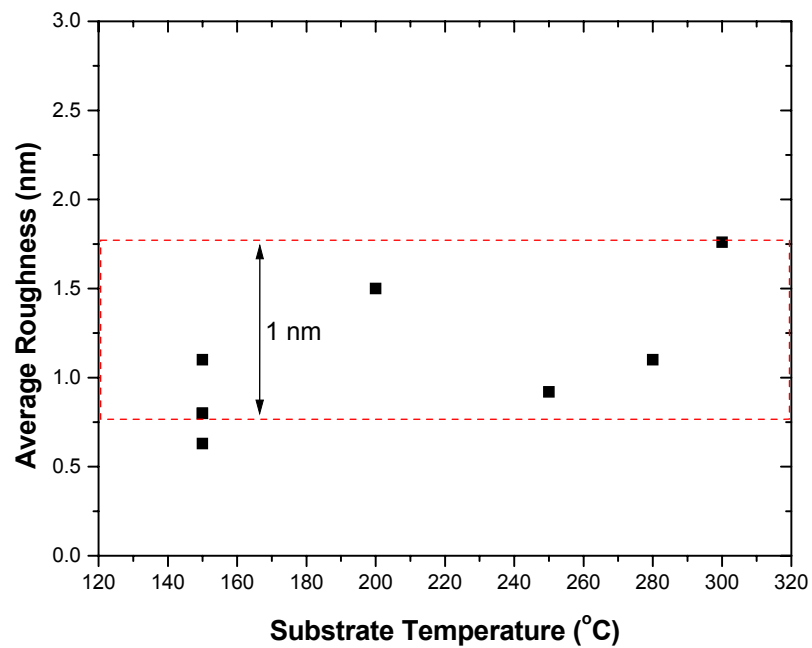


Figure 35. The average surface roughness as a function of the growth temperature

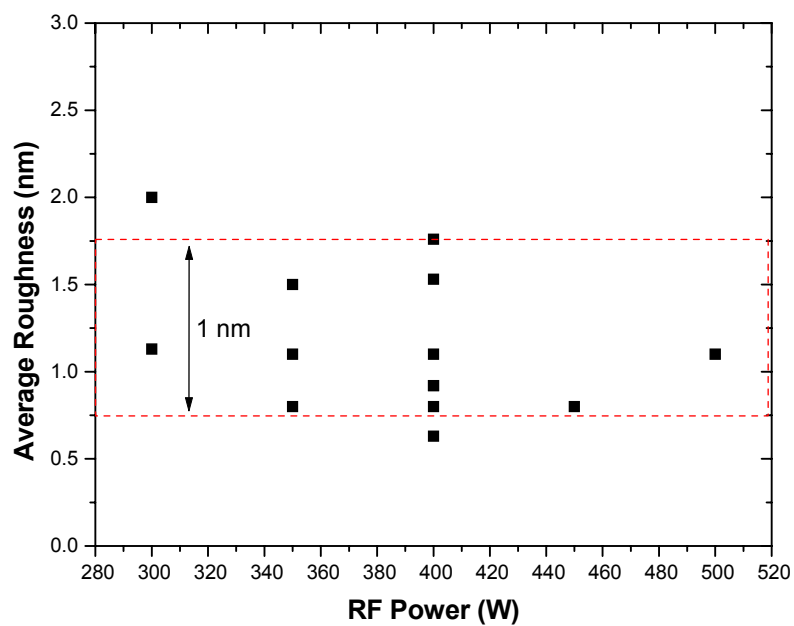


Figure 36. The average surface roughness as a function of the RF power used in the S atomic source

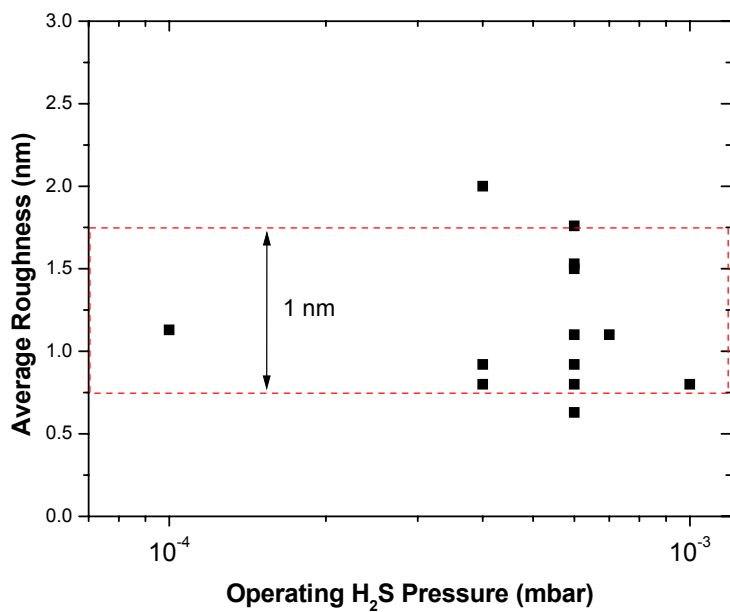


Figure 37. The average surface roughness is shown as a function of H₂S pressure used during growth

6.2.2 Stoichiometry of Grown Layers

The elemental composition is critical to the electronic quality of the grown material. Excess Cd or S may lead to the formation of defects and vacancies, which result in low mobility and high carrier concentration in the layers. In

Figure 38, Figure 39, and Figure 40, the layer composition, studied using AES depth profiling similar to those shown in Figure 29, is related to the experimental growth conditions. It should be noted that AES gives an approximate composition values. For every batch of samples, AES showed the same deviation for all the measured samples in the batch. This indicates that the deviation from the optimal 50 percent composition of S and Cd is mainly related to a measurement artifact. For all of the samples grown, AES showed a stoichiometric composition and an abrupt CdS/InP interface regardless of the experimental conditions used. This is an important observation since small changes in the experimental parameters may not result in alteration of the layer properties.

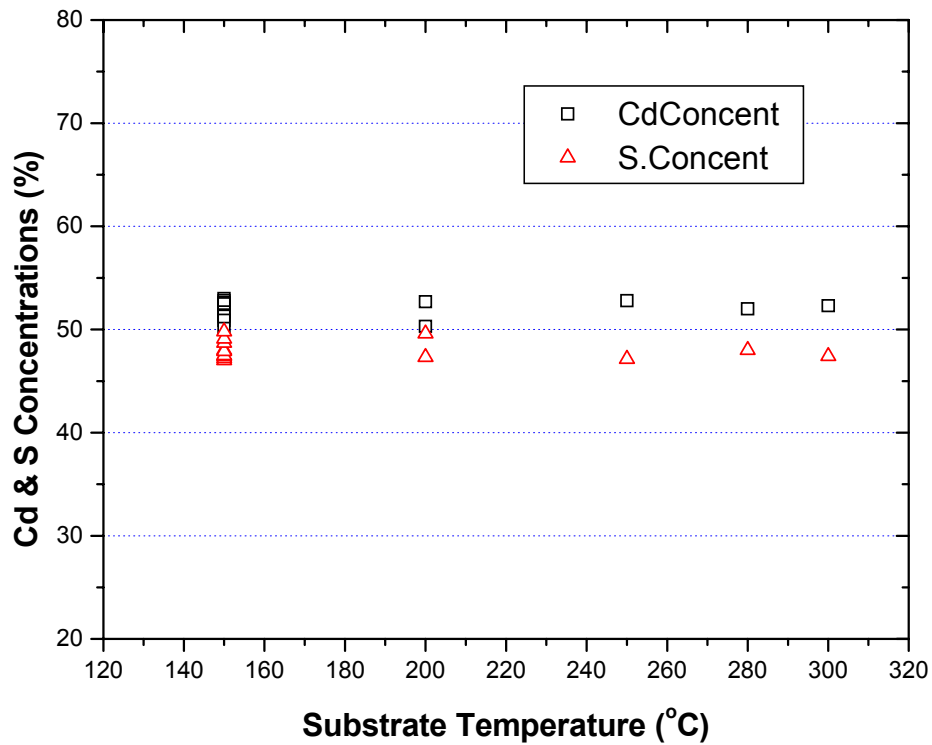


Figure 38. Cd and S concentration in layers grown in the temperature range from 150 to 300 °C

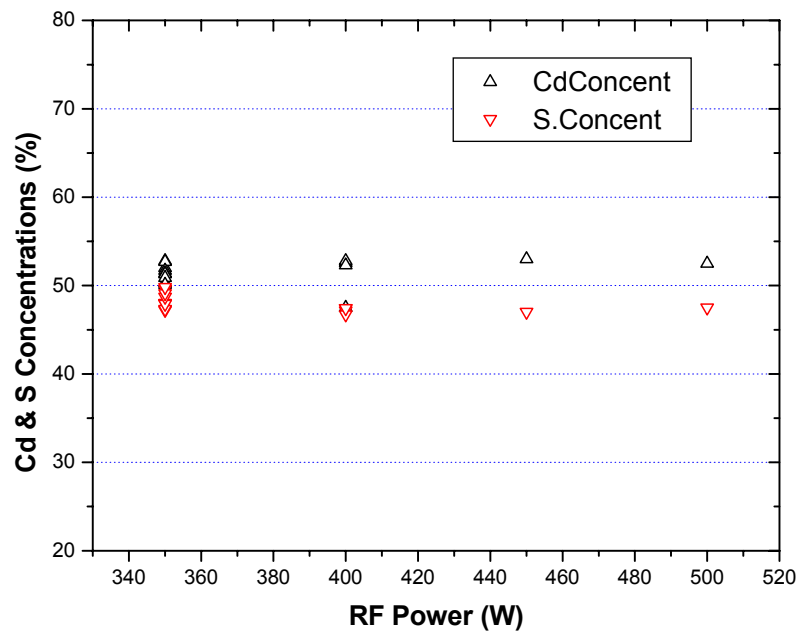


Figure 39. Dependence of layer compositions on the RF power used

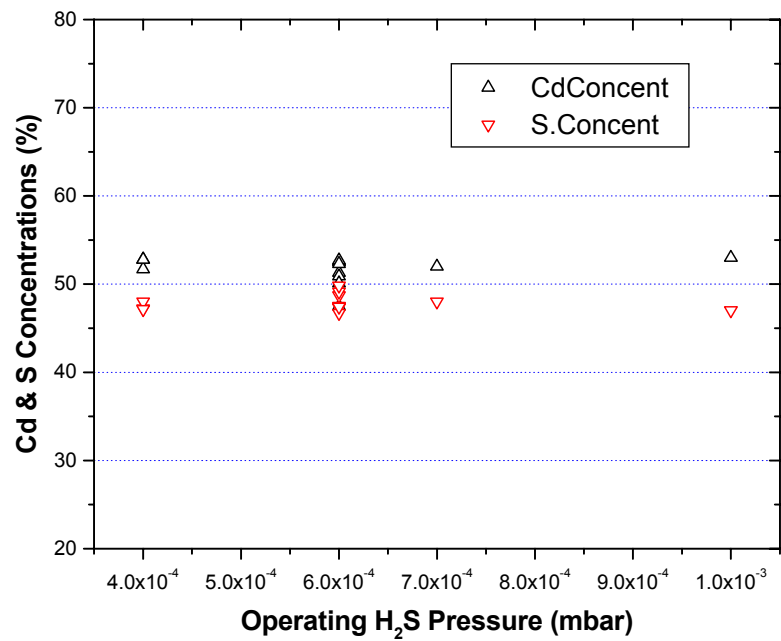
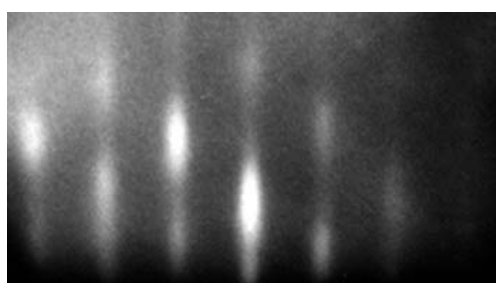


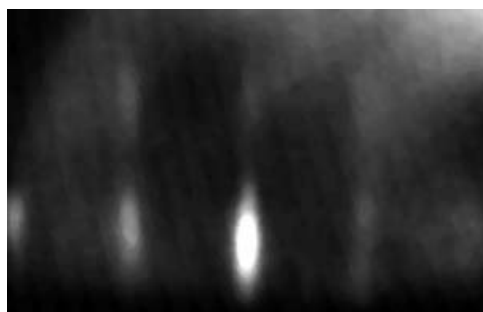
Figure 40. Dependence of layer composition on H_2S gas pressure during growth

7. DEPOSITION OF CdS USING CdS SOLID-SOURCE

Solid-source MBE (SS-MBE) using powder CdS as a single vapor source resulted in cubic growth similar to the case of gas-source MBE from H_2S and Cd. RHEED patterns, taken during the growth of CdS are shown in Figure 41. The patterns, which were taken along the [011] and [010], show growth of cubic CdS. No other phases were observed. In general, the surface morphology of layer grown by SS-MBE are rougher than layers grown by GS-MBE.



[011]



[010]

Figure 41. RHEED pattern from CdS grown by SS-MBE

The growth rate shown in Figure 42 varies exponentially with temperature and gives an activation energy of 1.7 eV, which is almost equal to the heat of formation for CdS (1.68 eV).

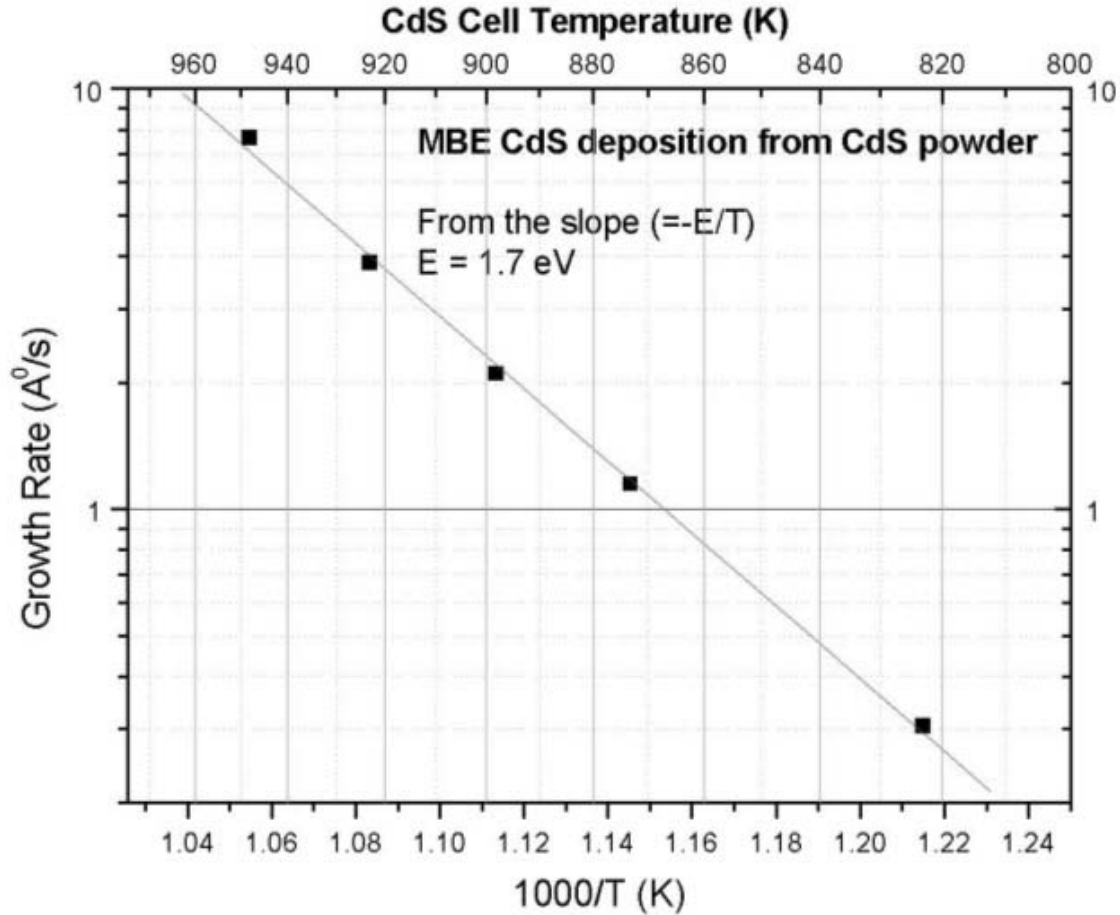


Figure 42. Deposition rate of CdS from CdS solid source

8. DEPOSITION OF LAS

We have built and operated all the three types of evaporation sources described in Section 4 of Part 1. These sources were based on (1) RF heating (Figure 16), (2) resistive heating (Figure 17), and (3) combined resistive and electron-beam heating (Figure 18). RF heating remains the most attractive method to achieve high temperature with minimal heat generation from the heating element (RF coil) and the least prone to failure. However, the limitations of our budget, time, and labor forced us to abandon this approach after the failure of our used RF power supply and the difficulties in matching the coil impedance to that of the power supply. The power supply operated on a single frequency (400 kHz) and high voltage (450 V), which made it difficult to obtain capacitors operating at the given voltage and frequency from commercial sources. The capacitors are needed for the matching network. Despite these difficulties, we have managed to build the matching network, but we lost the power supply at the early stages of experimentation. A solution to this problem would be to contract a specialized RF heating company for building the whole assembly including a high power (~3 to 4 kW), low-voltage, variable frequency power supply. We anticipate a price tag of \$30,000 to \$40,000 for the whole unit.

As an alternative, we have pursued the second approach (resistive heating) shown in Figure 17 (see Section 4, Part 1). However, the demands of high operating temperatures for La evaporation resulted in a frequent failure of the filament. Since La is sensitive to air, the repair had to be carried out in a controlled-atmosphere glove-box, which had to be purged with N₂ or Ar for at least 24 hrs prior to introducing the La cell into the glove box, making the repair into a lengthy and cumbersome process. As a result of these difficulties, we moved to the third alternative, shown in Figure 18. With this approach, we have achieved high operating temperature (>1300 °C) and we have made a few depositions, mostly after the end of the contract. There are still issues with the lifetime of the heater, but it is manageable compared to the second alternative. We believe that we have made some deposition of LaS (very thin layers), but have no information on the composition or the thickness of the layers.

9. SUMMARY

The work can be divided into two components, deposition of CdS on InP and deposition of LaS on CdS with the final goal of fabricating a high emission, planar, cold cathode.

For CdS, epitaxial cubic CdS layers were grown on InP(100) substrate using:

- (a) Ion-assisted growth using S⁺ ions generated from dissociation of H₂S gas in a single-grid ion-source operating at low energies (0 to ~ 800 V) and Cd evaporated from an effusion cell. Ion-assisted growth is viable method for deposition with the advantage of independent control over the ion flux, ion energy, and incidence angle. However, to achieve reasonable growth rates, the ion current must be high, which implies operating the ion-source at extreme conditions. This, in turn, results in a frequent failure of the ion-source, causing delays and reliability problems.
- (b) Hybrid gas-source/solid source MBE from atomic sulfur generated from H₂S and thermally evaporated cadmium. Epitaxial growth was achieved over the whole substrate temperature range (150-300 °C) investigated as indicated by RHEED observations. The deposition rate of CdS was primarily controlled by the Cd flux due to abundance of sulfur from the source gas (H₂S), and stoichiometric CdS films were formed for all growth temperatures and rates investigated. The CdS/InP interface was abrupt with no measurable interdiffusion to within the AES depth profile resolution, mainly due to the low growth temperatures used. AFM results indicate minimal CdS surface roughness (0.7-1.7 nm) at all substrate temperatures and layer thicknesses investigated, indicating a semi two-dimensional growth consistent with the observation of streaky RHEED patterns. The epitaxial growth on InP, low surface roughness, abruptness of interface, and the stoichiometric composition regardless of growth temperature and flux would enable fabrication of a new generation of optoelectronic devices and structures on InP.
- (c) Solid source MBE from a CdS powder evaporated using an effusion cell. The CdS-layers' crystal structure and stoichiometry were similar to those grown by the method in (b) above. However, the surface roughness is typically higher. In addition, the deposition rate showed direct correlation to the CdS vapor, as expected. Despite the slight drawback of higher surface roughness, the method is easier and more economical compared to (b).

For deposition of LaS, we have built a vacuum-tight, UHV compatible, movable, and compact evaporation source capable of high temperature operation ($>1300^{\circ}\text{C}$). Three methods were attempted for the deposition. However, the testing was not finalized on time due to the difficulties encountered during testing and the limited duration of the project. We have made some initial depositions, but have no quantitative measurements of the resulting layers.

Finally, a test station for field emission was built inside the MBE chamber for immediate testing of cold cathodes after growth, prior to exposure to air. The probe (anode) is made of highly doped, highly polished Si wafer coated with a $10\text{ }\mu\text{m}$ -thick layer of sol-gel. The sol-gel is patterned and etched to expose a fixed area of the Si wafer. During testing, the probe is brought in contact with the cold cathode and voltage is applied to the Si wafer (anode). This configuration makes the separation between the cold cathode and the anode fixed by the thickness of the sol-gel ($10\text{ }\mu\text{m}$ in this case). The close proximity eases the experiment, since much smaller voltage is needed to trigger emission compared to much larger separations used in typical field emission studies.

Finally, It is highly recommended that support for this project continues since most of the elements are in place and little more work is needed to test the concept.

ACKNOWLEDGMENT

The author gratefully acknowledge the financial support of the Air Force Research Laboratory under contract F33615-98-C-1205 administered by the Aerospace Components Division under Dr. Mark C. Calcaterra. Many thanks to Dr. P.D. Mumford for his support and helpful suggestions and to Jim Cook for an outstanding job in handling the contract, patience, and assistance with all administrative work.

REFERENCES

1. P.D. Momford and M. Cahay, *J. Appl. Phys.* 79, 2176 (1996)
2. P.D. Momford and M. Cahay, *J. Appl. Phys.*, 81, 3707 (1997)
3. M.-A. Hasan, G. Radnoczi, J.-E. Sundgren, and G.V. Hansson, *Surface Sci.* 236, 53 (1990).
4. M.-A. Hasan, G. Radnoczi, J.-E. Sundgren, and G.V. Hansson. American Vacuum Society 37th Annual Symposium and Topical Conferences, Toronto, Canada, October 8-12, 1990. (ABSTRACT)
5. M.-A. Hasan, G. Radnoczi, and J.-E. Sundgren. *Vacuum*, 41, 1121 (1990).
6. R.K. Parker and R.H. Abrams, "RF Vacuum Electronics: New Opportunities Invoking Microelectronic Capabilities," presented at GOMAC '92: The Emerging Technology Base, 1992.
7. D. H. Preist, "Planar Microwave Tubes and Circuits," in Electronics Engineers' Handbook, McGraw-Hill, New York, 1989.
8. J. L. Shaw, T. Jung, and H. F. Gray, IVMC 95, Portland, OR, USA, July 30-August 3, 1995, Technical Digest, p. 463.
9. H.-J. Fitting, Th. Hingst, E. Schreiber, and E. Geib, IVMC 95, Portland, OR, USA, July 30-August 3, 1995, Technical Digest, p. 468.
10. O Auciello, M. A. Ray, D. Palmer, J. Duarte, C. Ball, G. E. McGuire, and D. Temple, IVMC 95, Portland, OR, USA, July 30-August 3, 1995, Technical Digest, p. 473.
11. H. Adachi, IVMC 95, Portland, OR, USA, July 30-August 3, 1995, Technical Digest, p.479.
12. P. R. Davis, W. A. Mackie, C.H. Hinrichs, J. D. Parsons, J. M. King, IVMC 95, Portland, OR, USA, July 30-August 3, 1995, Technical Digest, p. 483.
13. Q. Chen, Y. Wang, X. Li, and J. Feng, IVMC 95, Portland, OR, USA, July 30-August 3, 1995, Technical Digest, p. 488.
14. A. Zur and T. C. McGill, *J. Appl. Phys.*, 55, 378 (1984).
15. S.L. Weng, A.Y. Cho, W.C. Mara, and P. Eisenberger, *Solid State Communication*, 34, 843 (1980).
16. H. Abad, B.T. Jonker, C. M. Cotell, and J. J. Krebs, *J. Vac. Sci. Technol. B*, 13, 716 (1995).
17. R. N. Bhargava, *Optoelectronics, Devices and Technology*, 7, 19 (1992).
18. P. J. Dean, *Phys. Status. Solidi A*, 81, 625 (1984).
19. T. Yao, *The Technology and Physics of Molecular Beam Epitaxy*, Editors M. G. Dowset and E. H. C. Parker, Plenum Press, NY (1985), p. 313.
20. J. M. DePuydt, H. Cheng, J.E. Potts, T. L. Smith, and S. K. Mohapatra, *J. Appl. Phys.*, 62, 456 (1988).
21. D. A. Cammack, K. Shahzad, and T. Marshall, *Appl. Phys. Lett*, 56, 845 (1990).

22. W. Stutius, *J. Cryst. Growth*, 59, 1 (1982).
 23. S. Fujita, M. Isemura, T. Sakamoto, and N. Yoshimura, *J. Cryst. Growth*, 86, 263 (1988).
 24. T. Yasuda, I. Mitsuishi, and H. Kukimoto, *Appl. Phys. Lett.*, 52, 57 (1988).
 25. K. Giapis, D. Lu, and K. Jensen, *Appl. Phys. Lett.*, 54, 353 (1989).
 26. M. A. Haase, J. Qin, J. M. DePuydt, and H. Cheng, *Appl. Phys. Lett.*, 59, 1272 (1991).
 27. W. Xie, D. C. Grillo, R. L. Gunshor, M. Kobayashi, G. C. Hua, N. Otsuka, H. Jeon, J. Ding, and A. V. Nurmikko, *Appl. Phys. Lett.* 60, 463 (1992).
 28. H. Jeon, J. Ding, W. Patterson, A. V. Nurmikko W. Xie, D. C. Grillo, M. Kobayashi, and R. L. Gunshor, *Appl. Phys. Lett.*, 59, 3619 (1991).
 29. P. O'Brian, J. R. Walsh, I. M. Watson, L. Hart, and S.R. P. Silva, *J. Crystal Growth*, 167, 133 (1996).
 30. M. Froment, M.C. Bernard, R. Cortes, B. Mokili, and D. Lincot, *J. Electrochem. Soc.*, 142, 2642 (1995).
 31. D. Lincot, R. Ortega-Borges, and M. Froment, *App. Phys. Lett.* 64, 569 (1994)
 32. MIT Wavelength tables, F. M. Phelps III, Vol. 2, p. 801, and 802, The MIT press, Cambridge, Massachusetts, USA, 1969.
- Also: A. N. Zaidel', V.K. Prokof'ev, S. M. Raiskii, V. A. Slavnyi, and E. Ya. Shreider, Tables of Spectral lines, IFI/Plenum, New York, 1970.

List of Anonyms and abbreviations

<u>ACRONYM</u>	<u>DESCRIPTION</u>
AES	Auger electron spectroscopy
AFM	atomic force microscopy
CARC	Cameron Applied Research Center
CdS	cadmium sulfide
EBE	electron beam evaporator
EIES	electron impact emission spectroscopy
EPD	etch pit density
FEA	Field emitter array
GS-MBE	gas-source molecular beam epitaxy
HCC	heterojunction cold cathode
InP	indium phosphide
IR	infrared
LaS	lanthanum sulfide
LED	Light emitting diode
LEED	low-energy electron diffraction
LEIAG	low-energy, ion-assisted growth
LN ₂	liquid nitrogen
MBE	molecular beam epitaxy
ML	monolayer
MOCVD	metal-organic chemical vapor deposition
MOMBE	metal-organic molecular beam epitaxy
PBN	pyrolytic boron nitride
R&D	research and development

RF	radio frequency
RHEED	reflection high-energy electron diffraction
SEM	scanning electron microscopy
SS-MBE	solid-source molecular beam epitaxy
TEM	transmission electron microscopy
UHV	ultrahigh vacuum
XPS	X-ray photoelectron spectroscopy